OECD/MCCI-2010-TR05

OECD MCCI Project
Category 4 Integral Test to Validate Severe Accident Codes:
Final Report

Rev. 1 - Final

November 2010

by:

M. T. Farmer, D. J. Kilsdonk, R. W. Aeschlimann, and S. Lomperski

Nuclear Engineering Division
Argonne National Laboratory
9700 S. Cass Avenue
Argonne, IL 60439 USA

Table of Contents

1. INTRODUCTION.....1
1.1 Background.....1
1.2 Objectives and Approach.....2
1.3 Related Studies.....4

2. FACILITY DESCRIPTION.....7
2.1 Test Apparatus.....7
2.2 Instrumentation and Data Acquisition.....16
2.3 Corium Composition.....19
2.4 Concrete Composition.....20

3. RESULTS AND DISCUSSION.....22
3.1 Summary of Test Operations.....22
3.2 Thermalhydraulic Results.....25
3.3 Posttest Examination Results.....37
3.4 Discussion.....41

4. SUMMARY AND CONCLUSIONS.....47

5. REFERENCES.....48

List of Figures

Figure **Page**

2-1 Schematic of CCI-6 Test Facility 8
2-2 Top View of Lower Test Section....8
2-3 Side View of Lower Test Section Showing Concrete Sidewall Sections....9
2-4 Details of the Basemat Nozzle Design 10
2-5 Nozzle Configuration on the Test Section Basemat Bottom Support Plate 10
2-6 Basemat Form Showing Nozzle Array Prior to Concrete Placement....11
2-7 CCI-6 Quench System 12
2-9 Test Section Top Flooding Water Supply System....13
2-8 Basemat Water Nozzle Supply System 14
2-10 Illustration of CCI-6 Crust Lance Assembly Mounted in Test Section....15
2-11 Plan View of Basemat Instrumentation Layout 17
2-12 Elevation View of Basemat Type C Thermocouple Locations 18
2-13 CCI Data Acquisition and Control Systems. 19
3-1 Power Supply Voltage and Power: Early Phase of the Test. 26
3-2 Power Supply Voltage and Power over the Entire Test....26
3-3 Melt Temperature Data from Basemat Type C “WCL” Array. 27
3-4 Melt Temperature Data from North Side Wall Type C “WN” Array....27
3-5 Melt Temperature Data from South Side Wall Type C “WS” Array. 28
3-6 Data from all Melt Temperature Thermocouples. 28
3-7 Melt Temperature Data from “WS” Array: Expanded Scale....29
3-8 Thermal Response of the Concrete Basemat at the Centerline....30
3-9 North Concrete Sidewall Thermal Response at +12.5 cm....31
3-10 South Concrete Sidewall Thermal Response at +12.5 cm....31
3-11 Basemat Axial Ablation Front Location....32
3-12 South Sidewall Radial Ablation Front Location....32
3-13 Comparison of Axial and Radial Ablation Depth Data versus Time. 33
3-14 Crust Lance Applied Load and Position vs. Time....34
3-15 CCI-6 Debris-Water Heat Flux (Top Flooding). 36

List of Figures (Contd.)

Figure **Page**

3-16 Integrated Heat Removal to Water and Heat Input to Melt from DEH. 36

3-17 Top View of Particle Bed After Removal of Upper Sidewall Sections.....37

3-18 Closeup Photograph of Material Removed from Particle Bed Over Fractured Crust 38

3-19 Views of the Debris After Particle Bed Removal (a) from the Top and (b) Closeup of the Volcanic Mound in the North-Central Region of the Debris as Viewed from the South 39

3-20 Face-on Views of (a) North and (b) South Concrete Sidewalls After Removal.....41

3-21 Views of Corium Debris Remaining Over the Basemat as Viewed from (a) North and (b) South.....42

3-22 Closeup Photograph of Fractured Crust Material after Removal from Test Section.....43

3-23 Rendering of Posttest Debris Configuration.....44

List of Tables

Table **Page**

1-1 Specifications for CCI-6 3

2-1 Type K Thermocouple Locations Used to Determine the Timing of Water Addition to the Test Section.....17

2-2 Post-Reaction Bulk Composition for CCI-6 Thermite 20

2-3 Detailed Pre- and Post-Reaction Compositions for CCI-6 Thermite 20

2-4 Engineering Composition of CCI-6 Siliceous Concrete.....21

2-5 Chemical Composition of Siliceous Concrete.....21

3-1 CCI-6 Event Sequence.....23

1.0 INTRODUCTION

1.1 Background

Ex-vessel debris coolability is an important light water reactor (LWR) technical challenge. For existing plants, resolution of this challenge will confirm the technical basis for severe accident management guidelines (SAMGs). For new reactors, understanding this challenge will help confirm the effectiveness of the design and implementation of new accident mitigation features and severe accident management design alternatives (SAMDAs). The first OECD-MCCI program conducted reactor material experiments focused on achieving the following technical objectives: i) provide confirmatory evidence and data for various cooling mechanisms through separate effect tests for severe accident model development, and ii) provide long-term 2-D core-concrete interaction data for code assessment and improvement.

Debris cooling mechanisms investigated as part of the first MCCI program included: i) water ingression through cracks/fissures in the core debris, ii) melt eruption caused by gas sparging, and iii) large-scale crust mechanical failure leading to renewed bulk cooling. The results of this testing and associated analysis provided an envelope (principally determined by melt depth) for debris coolability. However, this envelope does not encompass the full range of potential melt depths for all plant accident sequences. Cooling augmentation by additional means may be needed at the late stage to assure coolability for new reactor designs as well as for various accident sequences for existing reactors. In addition, the results of the CCI tests showed that lateral/axial power split is a function of concrete type. However, the first program produced limited data sets for code assessment. In light of significant differences in ablation behavior for different concrete types, additional data would be useful in reducing uncertainties and gaining confidence in code predictions.

Based on these findings, a broad workscope was defined for the follow-on MCCI program. The workscope was divided into the following four categories:

1. Combined effect tests to investigate the interplay of different cooling mechanisms, and to provide data for model development and code assessment purposes.

2. Tests to investigate new design features to enhance coolability, applicable particularly to new reactor designs.

3. Tests to generate two-dimensional core-concrete interaction data.

4. Integral tests to validate severe accident codes.

In addition to the experimental work, an analysis task was defined to develop and validate coolability models to form the basis for extrapolating the experiment findings to plant conditions.

As one of the steps required to satisfy these objectives, the Management Board (MB) approved the conduct of the first Category 4 Test. In particular, the following PRG recommendation was approved at the 5th PRG meeting which contains specifications for this test:

The PRG recommends that the OA design a 70 cm x 70 cm test, with two concrete side walls, using CEA siliceous concrete, 6 wt% concrete composition, early top flooding initiated when ablation is established and melt temperature has stabilized. The melt depth shall be 30 cm. The test will be designed for two specific phases. The first phase will provide for 30 cm of radial ablation and 25 cm for vertical ablation. In the event that the melt is not cooled down by top flooding during the first phase, a second and separate test phase will begin involving bottom flooding. This second phase will be initiated when axial ablation depth reaches 25 cm. The design should be mindful of the curing time of the concrete. The instrumentation should be refined to provide data on the water injection characteristics and melt temperature near the lateral walls.

1.2 Objectives and Approach

In response to the PRG mandate, a summary test plan for this sixth Core-Concrete Interaction (CCI-6) experiment was prepared [1], reviewed by the PRG, and subsequently approved for test conduct. Detailed specifications that were developed as part of the test planning process are provided in Table 1-1. The experiment approach was to incorporate an array of water nozzles into the core-concrete interaction test apparatus. The test section was enlarged to incorporate a 70 cm x 70 cm basemat. The initial melt depth was increased to 28 cm,[1] which corresponds to a thermite charge mass of 900 kg. The melt depth is noted to be slightly less than the 30 cm level requested by the PRG. The thermite charge was redesigned to include a reduced amount of concrete decomposition products (i.e., 6 wt %) relative to the previously performed CCI tests. The concrete sidewalls allow for 24 cm of lateral erosion, and the sidewall design was modified to include refractory MgO with a UO_2 pellet and U_3O_8 powder liner to stop the ablation if the 24 cm ablation depth was reached. The basemat and sidewalls also included an array of 45 concrete nozzles that were arranged on a 14 cm lateral pitch and were located at a uniform depth of 27.5 cm below the initial concrete basemat surface elevation. The nozzles were originally sealed at the top, and were fed with water from a common water supply tank that provided a static water head of nominally 10 kPa measured at the upper surface of the nozzles.

The planned operating sequence was to ignite the thermite and then provide 210 kW Direct Electrical Heating (DEH) to simulate decay heat. The concrete would then heat up and begin erosion. At this point, the cavity would be flooded from the top. If the melt did not cool, then the core-concrete interaction would continue until the 27.5 cm axial ablation depth was reached. At this point, the nozzles would open by erosion and thus initiate cooling by bottom water injection. The test would continue to operate until the melt was quenched, or the maximum axial ablation depth of 32.5 cm was reached. The experiment would then be terminated.

The CCI-6 experiment was carried out on 18 March 2010. Following a description of related studies in the next section, the balance of this final report provides a summary description

[1]The 28 cm melt depth is less than the 30 cm requested by the PRG. However, to achieve this depth the metal reaction byproduct in the melt would exceed that which, when oxidized, would produce sufficient H_2 to exceed 80 % of the lower flammability limit (LFL) in the test cell volume. This is one of the current safety limitations for the tests. Thus, the 28 cm melt depth (viz. 900 kg melt mass) was adopted to conform to the safety limitation and thereby minimize scheduling risks related to safety plan approvals.

of the test facility as well a presentation and discussion of results from the experiment. Full details are provided in a dedicated data report prepared for this test [2].

Table 1-1. Specifications for CCI-6.

Parameter	Specification
Corium	100 % oxidized PWR with 6 wt % siliceous concrete (CEA type)
Test section cross-sectional area	70 cm x 70 cm
Initial melt mass (depth)	900 kg (28 cm)[a]
Test section sidewall construction	24 cm thick concrete followed by MgO protected with a 2.5 cm thick layer of crushed UO_2 pellets and powder.
Test section basemat construction	48.1 cm thick concrete with an array of water injection nozzles embedded at a depth of 27.5 cm from the concrete top surface. Nozzles are uniformly pitched at a lateral spacing of 14.0 cm.
Sidewall maximum ablation depth	24.0 cm
Basemat maximum ablation depth	32.5 cm
System operating pressure	Atmospheric
Melt formation technique	Chemical reaction (~30 second reaction time)
Initial melt temperature	~2300 ºC
Melt heating technique	Direct Electrical (Joule) Heating
Melt heating method under dry cavity conditions	Constant power at 210 kW[b]
Melt heating method after cavity flooding	Constant voltage (preserves melt specific power density established prior to cavity flooding)
Criteria for top cavity flooding	Any combination of two different thermocouples located 2.5 cm within the concrete indicate arrival of the ablation front
Top flooding water inlet conditions	Inlet water temperature: 15 ºC Inlet water flowrate: ~ 2 liters/sec Sustained[c] water depth over melt: 25 ± 5 cm
Criterion for bottom water injection	Passive opening of nozzles once the axial ablation depth reaches 27.5 cm
Bottom injection water inlet conditions	Inlet water temperature: ~ 15 ºC Inlet water flowrate: 3.8 g/sec per nozzle, or 170 g/sec maximum if all 45 basemat nozzles are opened[d] Inlet water pressure at nozzle opening: 10±5 kPad
Test termination criteria	1) melt is quenched, or 2) maximum axial ablation depth of 32.5 cm is reached.

[a]Based on a calculated melt density of 6640 kg/m^3.

[b]Based on 150 kW/m^2 design heat flux to top, bottom, and two sidewall concrete surfaces (1.37 m^2 area), plus an additional 5 kW to compensate for a long-term heat losses of 10 kW/m^2 to MgO sidewalls (0.5 m^2 area).

[c]The water depth over the melt will be maintained in the indicated range until the nozzles open. Additional water will not be added from the top unless the test section plenum temperature climbs above saturation, indicating that the cavity has completely dried out.

[d]The 3.8 g/sec water injection flowrate limit corresponds to a local debris cooling rate of 500 kW/m^2 g/sec over the 14 cm x 14 cm surface area covered by one nozzle, assuming injection of room temperature water. The 170 g/sec injection flowrate limit would be reached if all 45 nozzles opened.

1.3 Related Studies

The purpose of this section is to identify and briefly discuss findings from related studies regarding ex-vessel melt coolability under the conditions of top flooding. This database includes experiments conducted with both low and high temperature simulants, and with prototypic reactor materials. Low temperature simulant experiments have been conducted by Theofanous et al. [3] to identify phenomena associated with melt coolability, while high temperature simulant experiments have been conducted at Sandia National Laboratories by Blose et al. [4,5] to investigate coolability with concurrent concrete erosion. In terms of reactor material testing, the COTELS [6,7] and MACE [8,9] experiment programs have been carried out to investigate coolability mechanisms under prototypic MCCI conditions. Results from both the simulant and reactor material testing programs are summarized below; more thorough discussions of the findings are provided by Farmer [9] and Sehgal [10].

To investigate fundamental phenomena associated with melt coolability, simulant material experiments were conducted by Theofanous, Liu, and Yuen [3]. In these tests, glycerin and liquid nitrogen were used to simulate the melt and overlying coolant, respectively. Gas sparging from MCCI was simulated by purging air through a porous plate located at the bottom of the apparatus. Fission product decay heat was simulated by the sensible heat deposited in the glycerin due to cooling of the purged gas from the inlet temperature to the melt pool temperature. Experiments were conducted in two different geometries; namely, cylindrical and square test sections. In the cylindrical tests, the diameters of the two test sections were 15 and 45 cm. For the rectilinear test sections, three different scales were investigated: 70 cm x 70 cm, 100 cm x 100 cm, and 120 cm x 120 cm. For the small scale tests conducted in the circular geometry, quench was not achieved due to the formation of wall-anchored crusts which inhibited the melt-coolant interaction. However, for the larger scale tests, quench was generally achieved. In particular, the data indicates that the time to quench increases with initial melt depth and decreases with increasing sparging rate. The principal mechanism leading to coolability in these experiments was volcanic eruptions. These eruptions lead to enhanced debris surface area available for contact with the overlying coolant. The same phenomenon was first identified through reactor material experiments under MCCI conditions [9].

Three melt coolability experiments were conducted at Sandia National Laboratories using high temperature simulants with sustained heating and concurrent concrete erosion. These experiments include the SWISS tests [4], conducted with stainless steel melts interacting with limestone/common sand concrete, and the WETCOR test [5] that was conducted with an oxide simulant interacting with Basaltic concrete. These tests also provided valuable data on debris coolability, but complete quench was not obtained in any of these experiments due in part to the formation of crusts that anchored to the test section sidewalls, eventually leading to decoupling of the melt pool from the crust as the core-concrete interaction proceeded downwards. However, these tests were quite valuable as they provided information on the effect of an overlying water pool on aerosol scrubbing during core-concrete interaction.

In terms of prototypic experiments, a total of 10 reactor material tests that investigated Fuel Coolant Interaction (FCI) and debris coolability were carried out within the framework of a

joint study between NUPEC and the National Nuclear Center (NNC) in Kazakhstan [6,7]. Each experiment was conducted in two phases; i.e., test series "B" investigated FCI aspects of the initial water injection onto molten corium, while the follow-on series "C" tests investigated the long-term aspects of MCCI under the conditions of continual water injection.

For these tests, based on the rate of steam transport to the condensation system, the steady-state melt/water heat flux was reported to range from 0.2 to 0.7 MW/m^2. In all cases, both the concrete sidewalls and base of the crucible were found to be eroded. In addition, an interstitial pebble bed formed at the interface of the core material and the concrete; the bed was composed of concrete decomposition products (presumably the aggregate). The depth of this pebble bed was found to increase with increasing ablation depth. The depth of the discolored concrete region surrounding the decomposed pebble bed was also found to increase with ablation depth. Posttest examinations revealed the important finding that crust anchoring to the concrete sidewalls with subsequent melt/crust separation did not occur for any of these tests. The absence of anchoring was presumably attributable to the sidewall decomposition that occurred.

The tests were classified in terms of the debris mass that was rendered in the form of a particle bed above the remaining corium layer. In particular, Case (1) corresponded to formation of a particle bed containing 20-40 wt % of the total debris mass, Case (2) corresponded to 70-80 wt % of the debris mass in the particle bed, while Case (3) corresponded to no particle bed formation. For experiments in which particle bed formation occurred (i.e., Cases (1)-(2)), the depth of the bed was found to increase with increasing basemat erosion depth, and with increasing melt specific power density. Particle bed depths ranged from 7 to 12 cm. In the Case (3) tests, no particle bed formation occurred; these experiments were characterized by comparatively lower power density. The mechanism by which these particle beds formed (e.g., entrainment by concrete decomposition gases) was not identified as part of this work. The coherent solidified corium layer remaining over the basemat was always found to contain cracks and crevices which axially spanned the depth of the layer. The test results indicate that water was able to penetrate into these cracks and crevices during the test, in addition to penetrating into the intervening gap formed at the sidewall corium-concrete interface due to sidewall erosion. In fact, for these tests the cooling mechanisms of water ingression through interstitial porosity and particle bed formation over the solidifying core material were of sufficient magnitude to effectively quench the core material and terminate the MCCI, as evidenced by thermocouple measurements in the basemat.

A series of large scale melt coolability experiments were conducted at Argonne National Laboratory as part of the Melt Attack and Coolability Experiment (MACE) [8,9]. The specific objectives of the program were to explore the possible benefits of massive addition of water to an MCCI already in progress insofar as: i) quenching and stabilizing the heat generating core melt, and ii) arresting or even terminating basemat ablation. Early tests M0 and M1b were conducted with 70 % oxidized PWR melt compositions, while the later tests M3b and M4 were conducted with fully oxidized core melts. Three tests in the matrix were conducted with limestone/common sand (LCS) concrete, while the fourth test was conducted with siliceous concrete. A principal parameter in the test matrix was test section lateral span, which was varied from 30 cm x 30 cm

up to 120 cm x 120 cm. Core melt masses in these various scale tests have ranged from 100 to 1800 kg.

The M0 experiment was conducted with a purely concrete test section, thereby allowing both axial and radial cavity ablation data to be obtained. This test provided early data on the effectiveness of the melt eruption cooling mechanism, with a substantial fraction of the initial core melt mass rendered in the form of a coolable bed by eruptions. Unfortunately, the crust anchored to the test section electrodes located along two opposing walls of the test section, and this eventually led to a configuration in which the melt had separated from the crust by the end of the experiment. Researchers thought that this experiment distortion may have precluded complete quench of the core debris. On this basis, the facility was redesigned to incorporate inert MgO sidewalls, thereby making it one dimensional, and the electrodes were recessed into the MgO sidewalls to reduce the surface area available for the crust to bond to. The balance of the integral experiments in the program (i.e., M1b, M3b, and M4) was conducted with this test configuration. Unfortunately, crust anchoring with subsequent melt-crust separation occurred in all these tests, and so a definitive demonstration of debris coolability was not obtained as a part of the MACE program.

Despite the crust anchoring issue, the MACE tests provided valuable insights on debris coolability phenomenology as well as datasets for code validation and assessment. In particular, four cooling mechanisms identified as part of this program included: i) bulk cooling, ii) water ingression into crust via inherent porosity, iii) melt dispersal into overlying water via fissures in the crust, and iv) mechanical breach of crust. Investigation of these various mechanisms has continued in the form of separate effect tests that have been conducted as part of the current OECD/MCCI program. Furthermore, parallel model development for these mechanisms has formed a technical basis for extrapolating the experiment findings to plant conditions. The test results as well as models point to the fact that debris coolability is enhanced under early cavity flooding conditions. The CCI-6 experiment documented herein was thus intended to examine the effectiveness of these various cooling mechanisms under this type of cooling scenario.

2.0 FACILITY DESCRIPTION

The overall facility design and test operating procedures for CCI-6 contained many elements that were similar to those used in the previous five tests [11-13]. However, several changes were made so that the test could serve as an integral experiment for validation of severe accident codes. In particular, the design was modified to include a 70 cm x 70 cm siliceous concrete basemat with two concrete side walls. Also, in contrast to the previous CCI tests, this test focused on coolability and therefore the cavity was flooded from above soon after the melt was produced. The initial melt depth was also modestly increased from the 25 cm level used previously to 28 cm.

Finally, the test was designed for operation in two distinct phases. The first phase consisted of a conventional 2-D core concrete interaction experiment that provided for 24 cm of lateral ablation and 27.5 cm of axial ablation. In the event that the melt did not cool down by top flooding during this first cavity ablation phase, a second and separate test phase would begin that involved bottom flooding. This phase would be initiated when the axial ablation depth reached 27.5 cm. The instrumentation was refined to provide data on the water injection characteristics, as well as the melt temperature near the concrete walls.

Additional details regarding the facility modifications are provided in the balance of this section. A complete description of the apparatus is provided in the test data report [2].

2.1 Test Apparatus

The CCI test facility consisted of a test apparatus, a power supply for Direct Electrical Heating (DEH) of the corium, a top flooding water supply system, a basemat nozzle water supply system, two steam condensation (quench) tanks, a ventilation system to complete filtration and exhaust the off-gases, and a data acquisition system. A schematic illustration of the overall setup is provided in Figure 2-1. The apparatus consisted of three rectilinear sidewall sections and a lid. The overall structure was 3.4 m tall. The two upper sidewall sections had a square internal cross sectional area of 50 cm x 50 cm.

The test section for containment of the core melt was located at the bottom of the apparatus. A top view of this component is shown in Figure 2-2, while a cross-sectional view of the non-electrode sidewalls is provided in Figures 2-3. The test section was enlarged to incorporate a 70 cm x 70 cm basemat. The concrete sidewalls allowed for 24 cm of lateral erosion, and the sidewall design was modified to include refractory MgO with a UO_2 pellet/U_3O_8 powder liner. This is the same inert sidewall design that has been successfully used behind the tungsten electrodes in all previous CCI tests. Thus, the sidewall design was intended to allow for continued test operation after the maximum lateral ablation depth of 24 cm was reached. In this manner, the core melt could be stabilized and allowed to proceed downwards to expose the water injection nozzles in the event that the melt was not successfully cooled by top flooding in the early part of the experiment, and/or rapid sidewall erosion occurred.

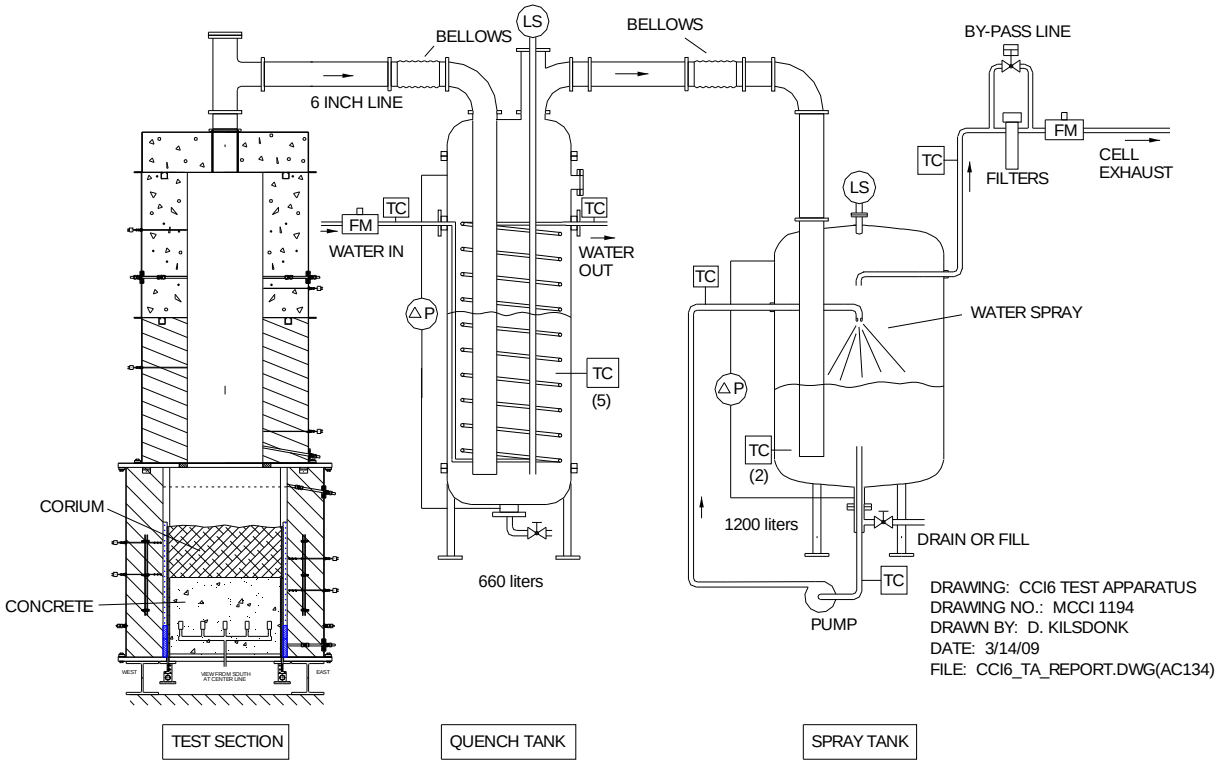

Figure 2-1. Schematic of CCI-6 Test Facility.

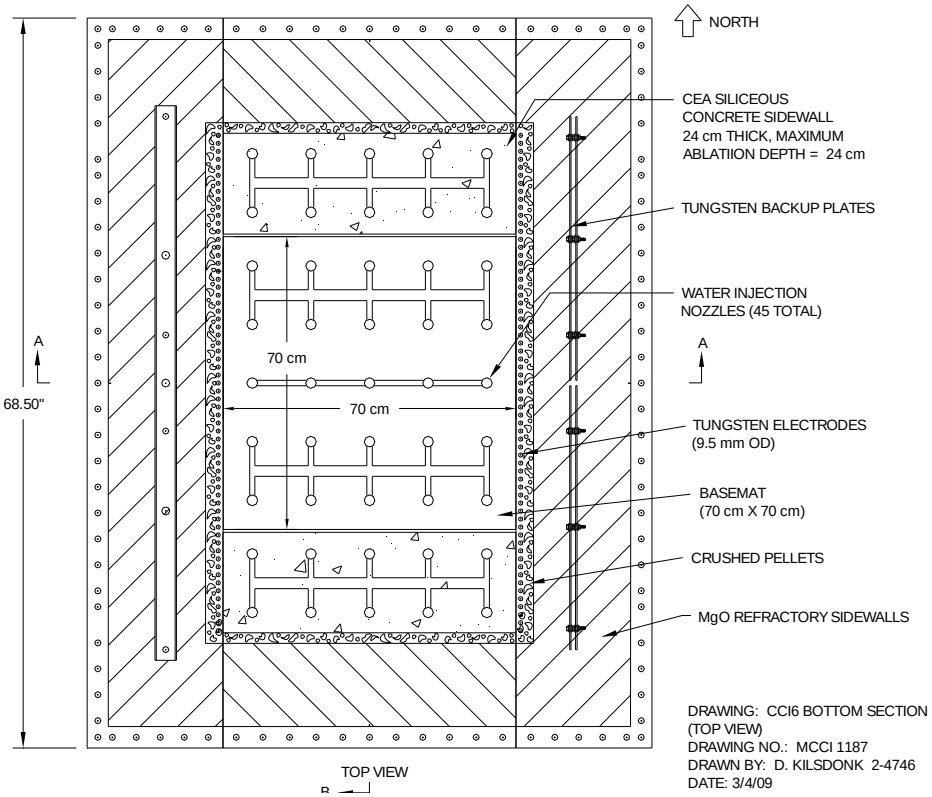

Figure 2-2. Top View of Lower Test Section.

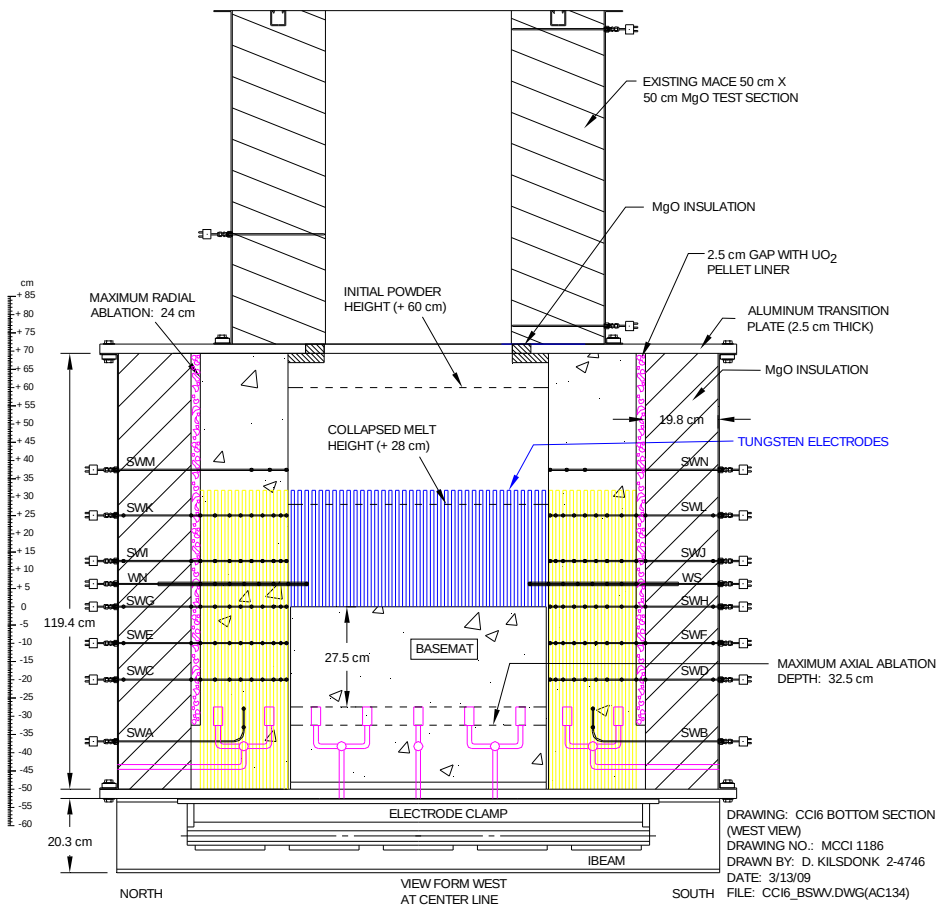

Figure 2-3. Side View of Lower Test Section Showing Concrete Sidewall Sections.

As shown in Figures 2-2 and 2-3, the basemat and sidewall designs were also modified to include an array of 45 concrete nozzles that were arranged on a 14 cm lateral pitch. Twenty five of the nozzles were configured in the basemat, while ten nozzles were configured in each of the two concrete sidewalls. The nozzle design details are shown in Figure 2-4, while the nozzle configuration on top of the basemat bottom support plate is shown in Figure 2-5. A photograph showing the concrete basemat form with the nozzles and a few of the basemat instruments installed prior to concrete placement is provided in Figure 2-6. The nozzles were all located at a depth of 27.5 cm below the initial concrete basemat surface elevation. The nozzles were sealed at the top with a PVC pipe caps, and all were fed with water from a common header tank that provided a static net pressure of nominally 10 kPa measured at the upper surface elevation of the nozzles. Once the corium melt reached the 27.5 cm axial ablation depth, the tops of the nozzles would be eroded through, thereby allowing passive water injection from below to begin the second phase of the experiment. At this point, the melt could be stabilized, or depending upon the extent of cooling, axial ablation could continue. If ablation continued, then the experiment would be terminated once the 32.5 cm axial erosion depth was reached. The porous concrete used in the nozzles was identical to that used in the SSWICS-12 test [14]; the formulation for this material was developed by Forschungszentrum Karlsruhe (FZK). However, as shown in Figure 2-4, the nozzle design was more robust compared to SSWICS-12 to ensure that these components could survive the concrete pouring process intact. Design robustness was not an

issue in terms of whether or not the nozzles would open once the melt front arrived since the melt was continuously heated. Each nozzle was electrically isolated from the test section so that an electrical shorting path could not develop once the melt contacted two or more nozzles.

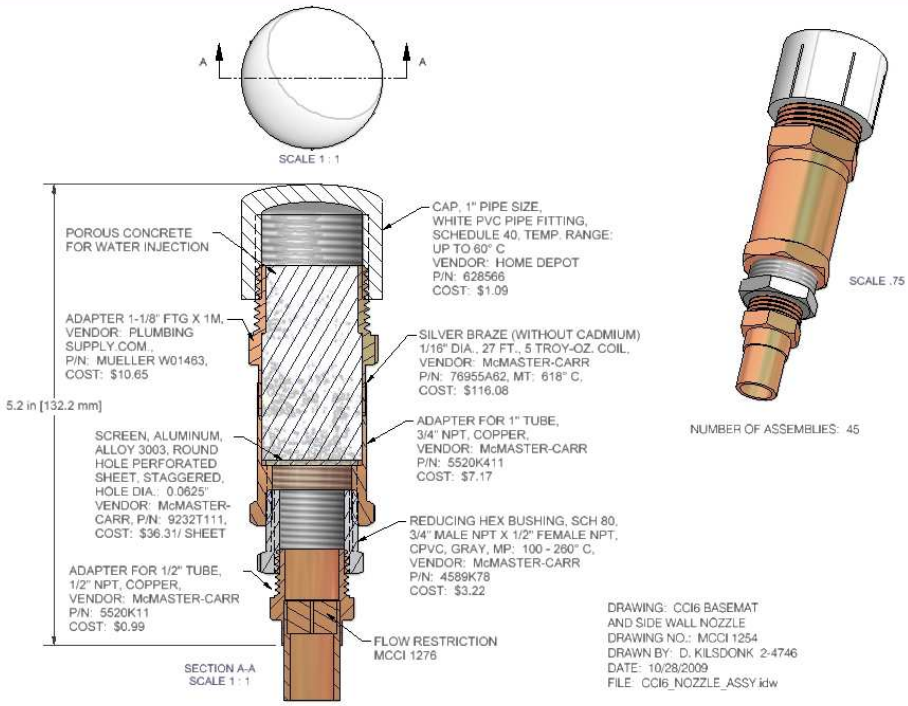

Figure 2-4. Details of the Basemat Nozzle Design.

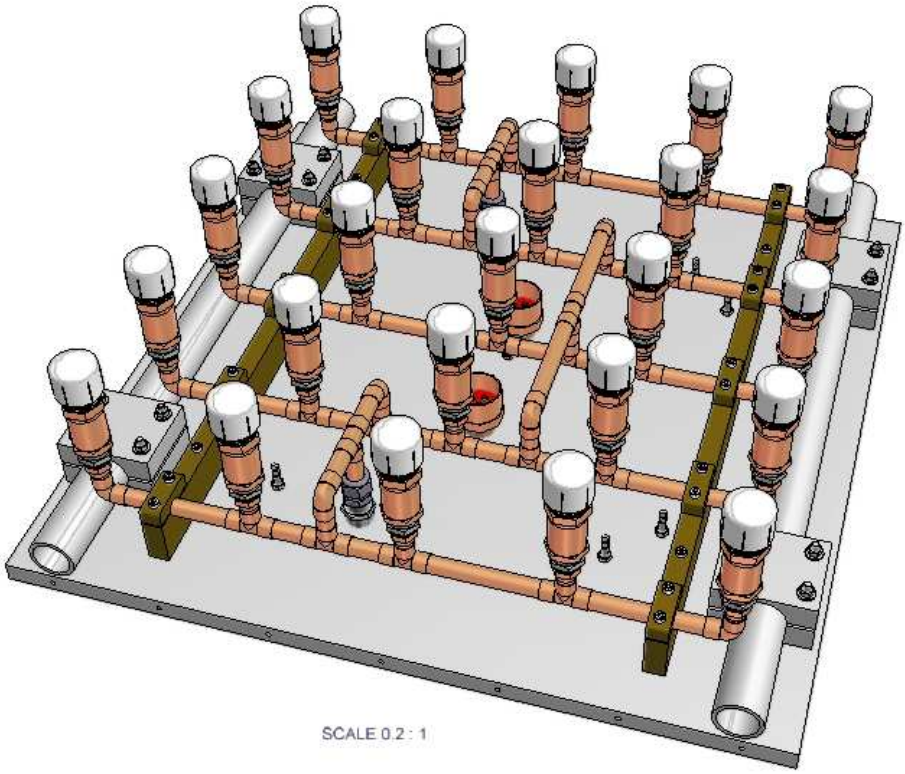

Figure 2-5. Nozzle Configuration on the Test Section Basemat Bottom Support Plate.

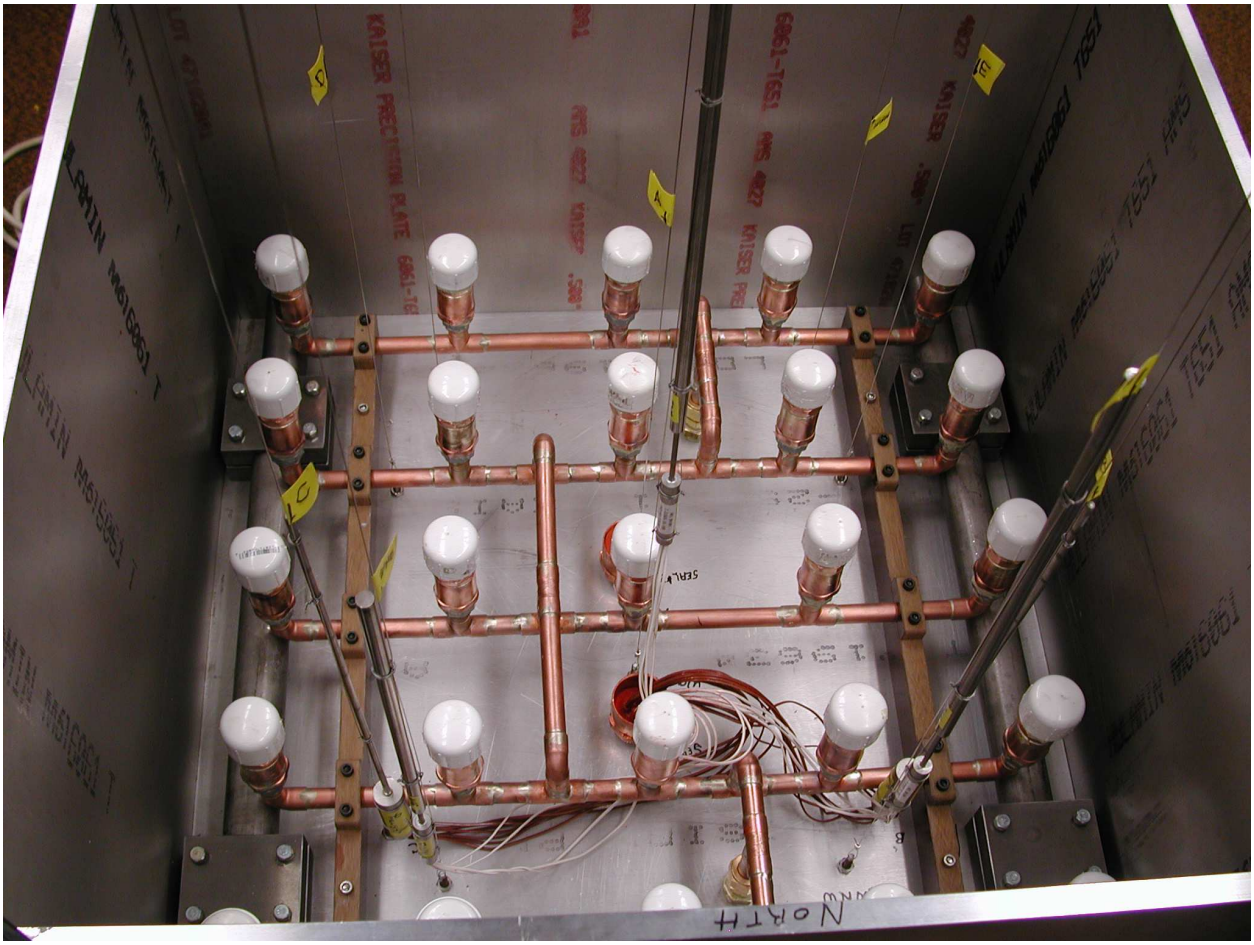

Figure 2-6. Basemat Form Showing Nozzle Array Prior to Concrete Placement.

As shown in Figures 2-2 and 2-3, the sidewalls of the lower test section were contained within a flanged steel form that was used to secure the unit to the balance of the existing test section components with an aluminum transition plate. The flanges allowed the lower sidewalls to be disassembled to reveal the solidified corium following the test. As previously noted, a layer of crushed UO_2 pellets and U_3O_8 powder was used to protect the interior surface of the MgO sidewalls against thermo-chemical attack by the corium. For the electrode sidewalls, molybdenum and tungsten plates were embedded in the MgO to stop erosion in case the UO_2/U_3O_8 protection layer failed. Multi-junction Type K and Type C thermocouple assemblies were cast within the sidewalls so that the time-dependent heat loss from the melt could be calculated from the local temperature gradient and the thermal conductivity of the MgO.

The melt was produced through an exothermic chemical reaction yielding the target mass over a timescale of ~ 30 seconds. After the chemical reaction, DEH simulating decay heat was applied through two banks of tungsten electrodes. As shown in Figure 2-2, the electrodes lined the interior surfaces of the two opposing MgO sidewalls. The electrodes were 9.5 mm in diameter and aligned in a row with a pitch of 1.9 cm. They were attached by copper clamps and water-cooled buss bars to a 560 kW AC power supply. The electrodes spanned a total width of 120 cm on each sidewall of the lower section. At the start of the experiment, the electrical

current was drawn through the center, 70 cm-wide section of electrodes that were in direct contact with the melt. As the test progressed and the concrete sidewalls were eroded, additional electrodes would be exposed to the corium. Current would be drawn through these newly exposed heating elements, thereby maintaining a uniform internal heat pattern in the melt over the course of the experiment. With the overall electrode span of 120 cm, the entire 24 cm of lateral sidewall erosion could be accommodated on both sides of the test section while ensuring that the entire melt cross-sectional area was in contact with the electrodes.

A few minutes after the melt was formed, ablation of the concrete basemat and sidewalls would commence. As shown in Figure 2-1 a large (15 cm diameter) gas line was used to vent the helium cover gas and the various gas species arising from the core-concrete interaction (i.e., CO, CO_2, H_2O, and H_2) into two adjacent quench tanks that were partially filled with water (see Figure 2-6). In the early initial phase of the experiment when the cavity was dry, the tanks served to cool the off-gases and filter aerosols generated from the core-concrete interaction. After the cavity was flooded, the tanks served to condense the steam and, based on the measured condensation rate, provide data on the corium cooling rate. In either case, the helium covergas and non-condensables (CO, CO_2, and H_2) passed through the tanks and were vented through an off gas system that included a demister and filters. The gases were eventually exhausted through the containment ventilation system and a series of high efficiency filters before finally being released from the building stack.

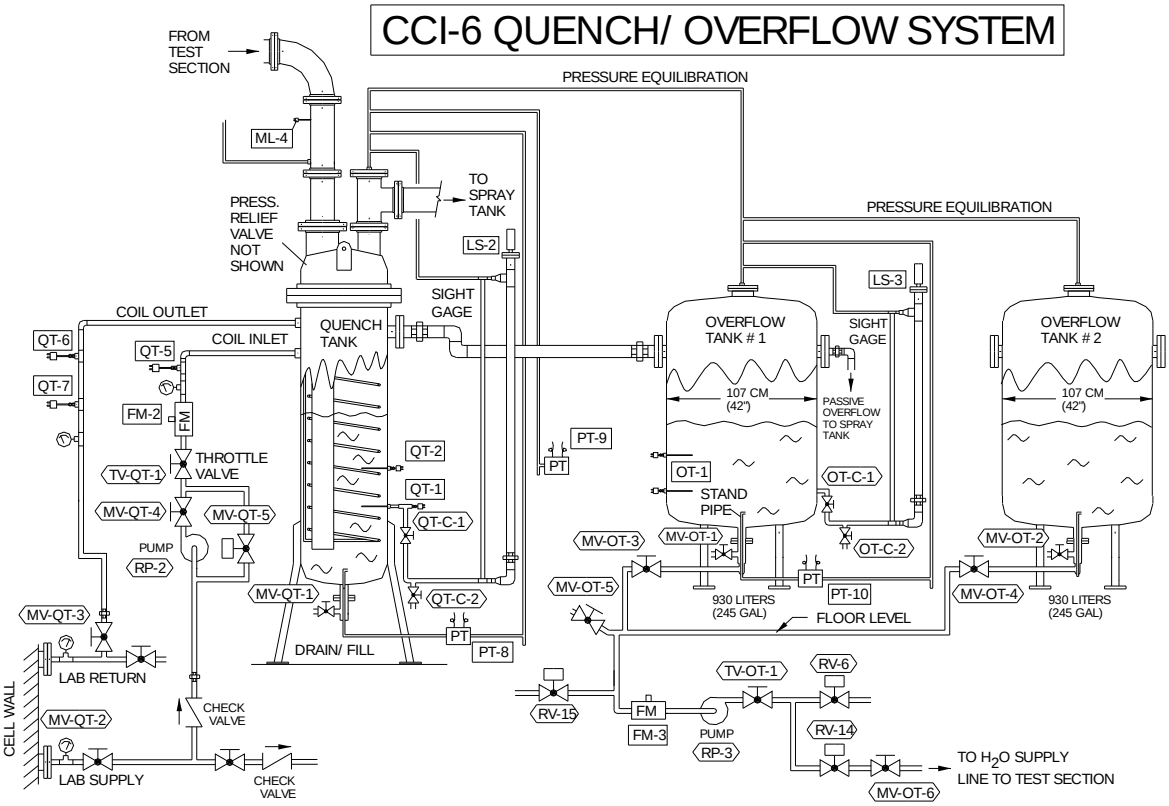

Figure 2-7. CCI-6 Quench System.

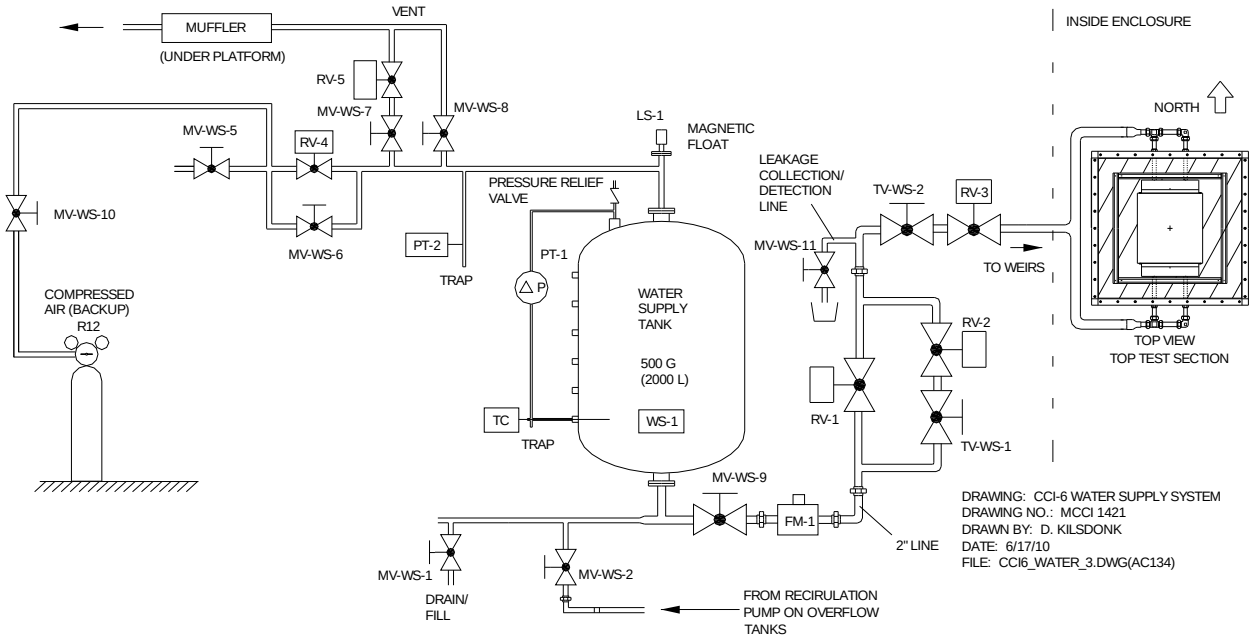

Figure 2-8. Test Section Top Flooding Water Supply System.

Soon after concrete erosion began, the cavity was flooded using an instrumented water supply system. During this stage of the test, the water entered the test section through two weirs located in the opposing (non-electrode) sidewalls of the top test section. The water supply system is shown in Figure 2-8. The supply tank was pressurized and water was injected using gas pressure as the driving force to push water through the interconnected piping to the test section weirs. Makeup water was periodically added to maintain the water level in the test section at nominally 25 ± 5 cm. This was an increased scale test, and so the system was set up to recycle water from the quench system overflow tanks to the water supply tank. This alternative flow path is shown in Figures 2-7 and 2-8.

A schematic illustration of the basemat nozzle supply system is shown in Figure 2-9. As concrete erosion proceeded, the point would eventually be reached at which the porous concrete nozzles in the basemat would open by ablation. When the axial ablation depth reached a predefined level, the isolation valves that separated the nozzle header tank from the nozzles would be opened (i.e., valve RV-INJ-BASEMAT and RV-INJ-PLENUM in Figure 2-9) in preparation for water injection from below. The total head included that required to offset the melt hydrostatic head, which was estimated as ~ 23.6 kPa[2]. Thus, the header tank was configured in the test cell to provide a static water height of 3.45 m to the nozzles. The plenum of the header tank was attached by a 1.3 cm ID pressure equilibration line to the test section plenum to ensure that the proper head was maintained as the test section plenum pressure fluctuated. As the quench process progressed, makeup water to the header tank would be

[2]Melt head at the time of nozzle opening was estimated to be 23.6 kPa, which included the 18.3 kPa head due to the initial 28 cm collapsed melt depth (melt density assumed to be 6640 kg/m^3), plus an additional 5.6 kPa of head from erosion of 27.5 cm of concrete (concrete density assumed to be 2270 kg/m^3, and 13.74 wt% of the concrete mass was lost due to liberation of the CO_2 and H_2O from the concrete. See Table 2-4 for concrete composition).

provided automatically by a water supply line that included a float switch so that the net head would be maintained in the range of 10±0.1 kPad. The water supply line to the nozzles was instrumented with a flowmeter to measure the total water injection flowrate. The flowrate would achieve a peak value of 170 g/sec (10 lpm) if all 45 nozzles completely opened during the test and there was effectively no hydraulic resistance offered by the debris downstream of the nozzle exits. After bottom water injection was initiated, additional water would only be added from the top if the test section plenum temperature started to rise significantly above saturation, indicating that the top coolant layer had been evaporated. This step would be taken to prevent damage to the upper internals from highly superheated steam that is produced by bottom flooding in the early stages of the transient before the bulk melt temperature has declined significantly.

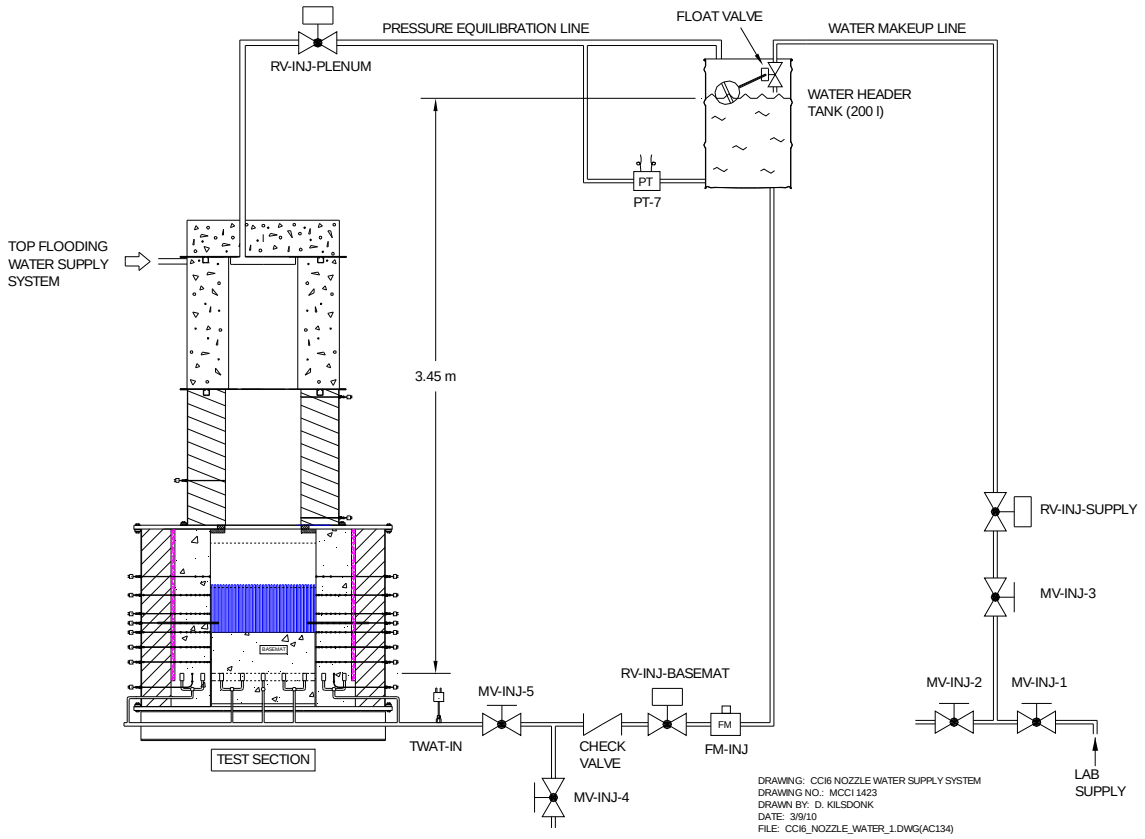

Figure 2-9. Basemat Water Nozzle Water Supply System.

After a specified time with water present in the cavity, the option was provided to break the crust formed at the melt-water interface with an insertable crust lance to obtain data on the crust breach cooling mechanism. An illustration of the lance installed in the test section is shown in Figure 2-10. The lance was made from 2.54 cm diameter, 304 stainless steel rod with a pointed tip. The lance contained an electrical isolation hub so that there was no need to terminate power input to the melt during the crust loading procedure. As shown in Figure 2-10, the driving force for the lance was simply a 450 kg dead weight that was remotely lowered with the crane during the test. The lance was equipped with a load cell to measure applied load and a displacement transducer to measure lance tip elevation in the test section.

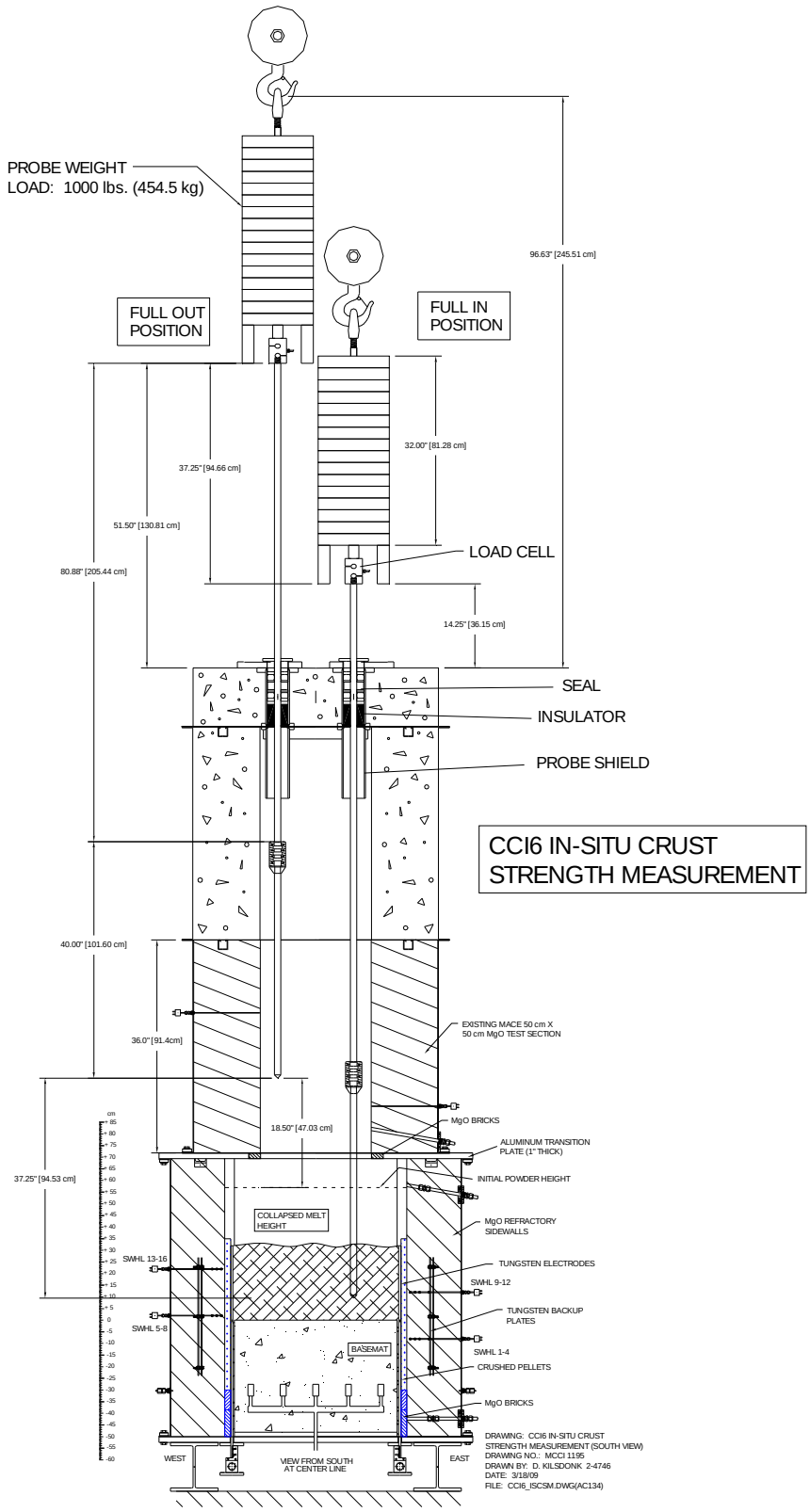

Figure 2-10. Illustration of CCI-6 Crust Lance Assembly Mounted in Test Section.

2.2 Instrumentation and Data Acquisition

The CCI-6 facility was instrumented to monitor and guide experiment operation and to log data for subsequent evaluation. Principal parameters that were monitored during the course of the test included the power supply voltage, current, and gross input power to the melt; melt temperature and temperatures within the concrete basemat and sidewalls; crust lance position and applied load; supply water flow rate to the test section weirs as well as to the concrete nozzles; water volume and temperature within the test apparatus, and water volume and temperature within the quench system tanks. Other key data recorded by the DAS included temperatures within test section structural sidewalls, off gas temperature and flow rate, and pressures at various locations around the system. Measurement uncertainties for all instruments are provided in the test data report [2].

The concrete basemat and sidewalls for CCI-6 were instrumented to monitor melt temperature during both the top flooding and bottom water injection phases of the test using multi-junction Type C thermocouples in tungsten thermowells. In addition, a two-color optical pyrometer was used to measure the debris upper surface temperature before water addition and during periods when aerosol production did not optically occlude the view of the surface. Multi-junction Type K thermocouples cast directly in the basemat and sidewalls were also used to track the progression of the concrete ablation front. Plan and elevation views of the basemat thermocouple layout are provided in Figures 2-11 and 2-12, while the sidewall thermocouple layout is shown in Figure 2-3. Note that the thermocouple junction locations were spread out to provide melt temperature and ablation front location data over the full range of possible concrete ablation depths. As shown in Figure 2-3, for CCI-6 the first junctions of the laterally mounted Type C thermocouples in the concrete sidewalls were extended out 5.0 cm from the concrete surface to provide data on melt temperature adjacent to the walls early in the experiment.

A further instrumentation requirement[3] was to provide sufficient thermocouple planar density to detect concrete ablation to a depth of 2.5 cm into the concrete basemat and/or sidewalls, since the cavity was to be flooded when any combination of two thermocouples at this depth indicated arrival of the ablation front (see Table 1-1). The positions of the various thermocouples that were installed to achieve this detection capability are shown in Table 2-1.

Other significant instrumentation included a stationary (lid mounted) video camera for observing physical characteristics of the core-concrete interaction.

All data acquisition and process control tasks were managed by a PC executing LabVIEW 8.2 under Windows XP. Sensor output terminals were connected inside the test cell to model HP E1345A 16-channel multiplexers, which were integrated into a mainframe chassis in groups of eight. An illustration of the DAS setup is provided in Figure 2-13. The multiplexers directed signals to an HP E1326B 5 ½ digit multimeter incorporated into each chassis. Three independent 128 channel systems were used for a total capacity of 384 channels.

[3] See Action 6.3 from the Minutes of the 6th OECD/MCCI-2 PRG meeting held at Argonne 20-21 April, 2009.

Table 2-1. Type K Thermocouple Locations Used to Determine the Timing of Water Addition to the Test Section.

Instrument Name	Test Section Concrete Component	Planar Position	Depth Below Concrete Surface
A-2	Basemat	Centerline	2.5 cm
B-2	Basemat	Northwest quadrant	2.5 cm
C-2	Basemat	Northeast quadrant	2.5 cm
D-2	Basemat	Southeast quadrant	2.5 cm
E-2	Basemat	Southwest quadrant	2.5 cm
SWG-2	North wall	Lateral centerline, 0.0 cm above basemat	2.5 cm
SWI-2	North wall	Lateral centerline, +12.5 cm above basemat	2.5 cm
SWK-2	North wall	Lateral centerline, +25.0 cm above basemat	2.5 cm
SWH-2	South wall	Lateral centerline, 0.0 cm above basemat	2.5 cm
SWJ-2	South wall	Lateral centerline, +12.5 cm above basemat	2.5 cm
SWL-2	South wall	Lateral centerline, +25.0 cm above basemat	2.5 cm

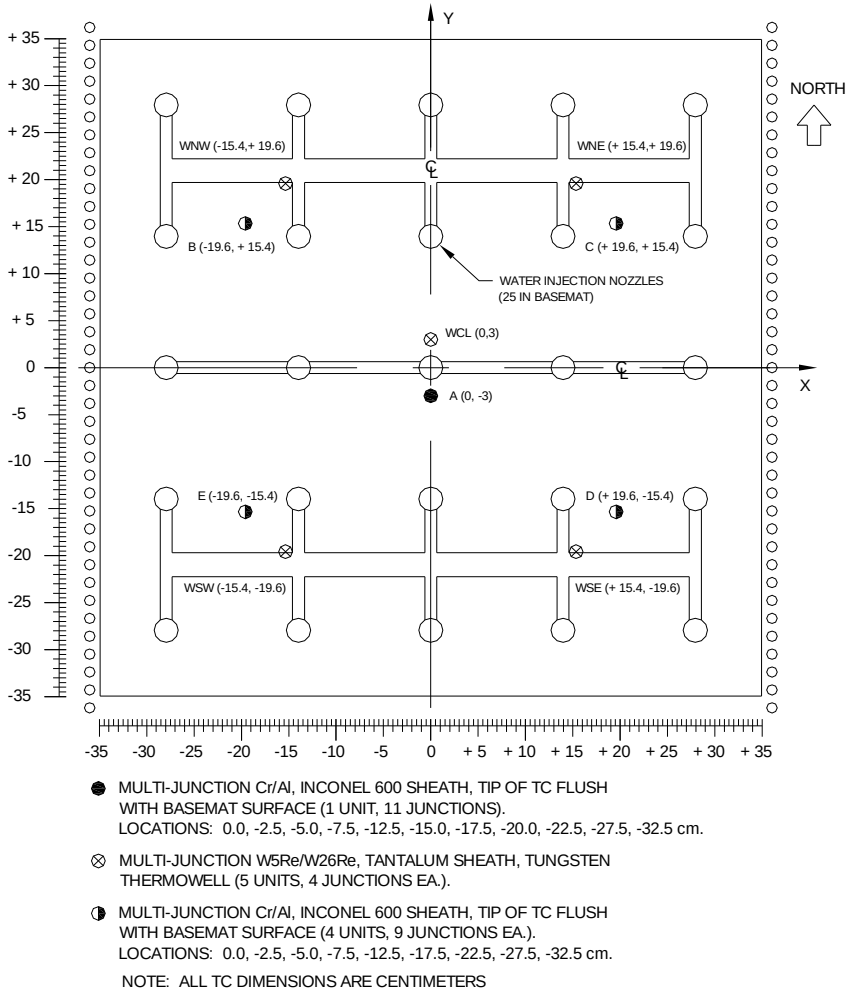

Figure 2-11. Plan View of Basemat Instrumentation Layout (dimensions are in cm).

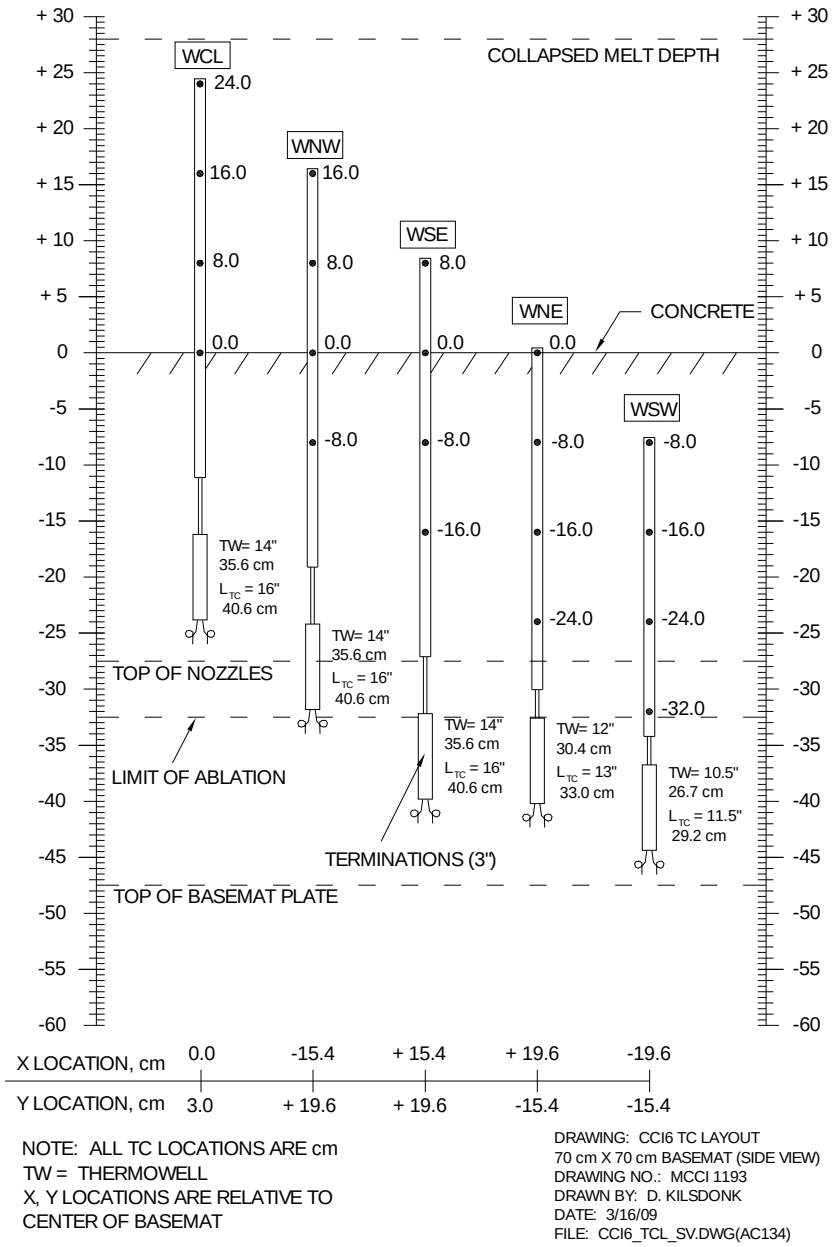

Figure 2-12. Elevation View of Basemat Type C Thermocouple Locations.

Signal noise was reduced by the digitizer through integration over a single power line cycle (16.7 ms). The digitized sensor readings were routed from the test cell to the PC in the control room via two HP-IB extenders. The extenders allowed the ASCII data from the HP to be sent through the cell wall over a BNC cable. The extender within the control room then communicated with a GPIB card within the PC. This configuration also permitted remote control of the multimeter through LabVIEW.

Integration of the signal over the period of a power line cycle limited the speed with which the multiplexer could scan the channel list. The minimum time for the digitizer to scan

the channel list was ~1.7 s (16.7 ms • 100 channels/chassis for this test). Though the three systems operated independently, implying the ability to update all 300 channels in roughly two seconds, the actual time required for the update was about 5.5 s.

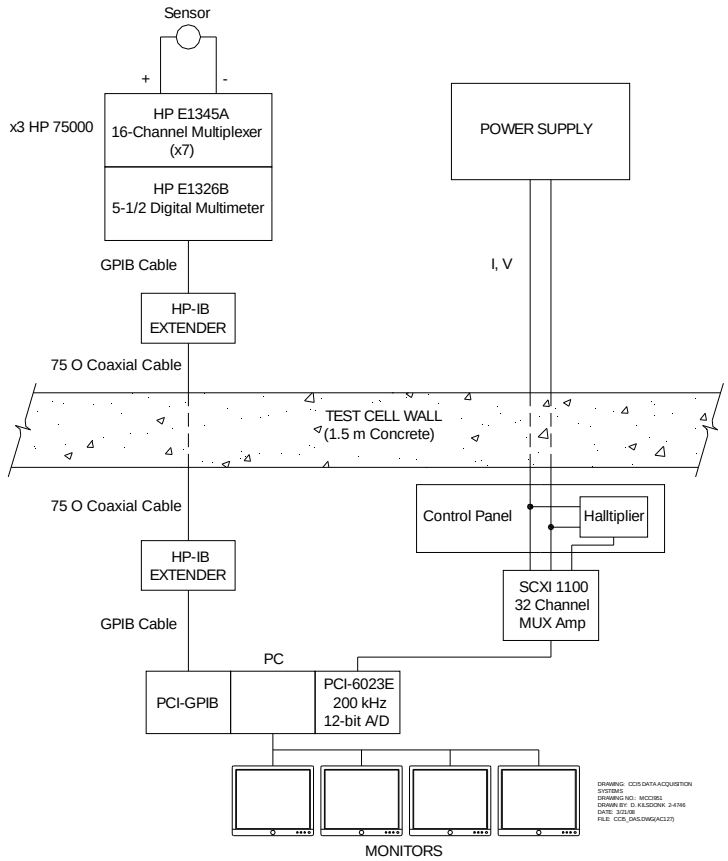

Figure 2-13. CCI Data Acquisition and Control Systems.

2.3 Corium Composition

As shown in Table 1-1, the corium oxide phase composition for CCI-6 was specified to contain 6 wt % calcined siliceous concrete as an initial constituent. As part of the developmental work for this test, a specific thermite was developed to produce this particular melt composition. The thermite reaction is of the form:

$$1.22U_3O_8 + 3.3Zr + 0.649Si + 0.531SiO_2 + 0.017Mg + 0.25CaO + 0.084Al + 1.866CrO_3 \rightarrow$$

$$3.66UO_2 + 3.3ZrO_2 + 1.18SiO_2 + 0.017MgO + 0.25CaO + 0.042Al_2O_3 + 1.866Cr;$$

$$Q = -269.08 \text{ kJ/mole } (1.756 \text{ MJ/kg});$$

$$T_{adiabatic} = 2692 \text{ °C}; T_{actual} \sim 2310 \text{ °C}$$

The composition of the melt produced from this reaction is summarized in Table 2-2, while the detailed pre- and post-reaction compositions are provided in Table 2-3. The actual reaction temperature shown under the above chemical reaction was determined by igniting a 1 kg sample in a crucible and measuring the peak temperature with a Type C thermocouple.

Note that the pre- and post-reaction compositions shown in Tables 2-2 and 2-3 do not include the additional mass of crushed UO_2 pellets and U_3O_8 powder that were used to line the test section MgO sidewalls. Experience has shown that this material does not participate in the initial exothermic chemical reaction, and remains essentially intact as a protective layer during the ensuing core-concrete interaction. Thus, this material is not included in the initial melt mass estimate for the test.

The thermite powders were packed into the test section in a large, 1.7 mil aluminized Saran bag that was pre-installed over the basemat to prevent water absorption by CrO_3 and concrete oxides (principally CaO and SiO_2), since these constituents are hygroscopic. As an additional measure to prevent moisture infiltration into the thermite from the concrete, the basemat and sidewalls were completely covered with continuous sheets of Saran film before thermite loading.

Table 2-2. Post-Reaction Bulk Composition for CCI-6 Thermite.

Constituent	Wt%
UO_2	62.51
ZrO_2	25.67
Calcined Concrete	5.68[a]
Cr	6.14

[a]Calcined siliceous concrete, consisting of 79.0/0.9/15.6/4.5 wt% SiO_2/MgO/CaO/Al_2O_3

Table 2-3. Detailed Pre- and Post-Reaction Compositions for CCI-6 Thermite.

Constituent	Reactant		Product	
	Wt %	Mass, kg	Wt %	Mass, kg
U_3O_8	64.99	584.91	-	-
UO_2	-	-	62.50	562.50
Zr	18.99	170.91	-	-
ZrO_2	-	-	25.67	231.03
Si	1.15	10.35	-	-
SiO_2	2.02	18.18	4.49	40.41
Mg	0.01	0.09	-	-
MgO	-	-	0.04	0.36
Al	0.14	1.26	-	-
Al_2O_3	-	-	0.27	2.43
CaO	0.89	8.01	0.89	8.01
CrO_3	11.81	106.29	-	-
Cr	-	-	6.14	55.26
Total	100.00	900.00	100.00	900.00

2.4 Concrete Composition

As shown in Table 1-1, the composition of the CCI-6 concrete basemat and sidewalls was specified to be of the siliceous type. The engineering composition for this particular concrete is shown in Table 2-4. The sand and aggregate for the mix were supplied by CEA as an in-kind contribution to the program. The chemical composition of this concrete is shown in Table 2-4.

The composition was determined[4] based on chemical analysis of the archive sample that was produced when the components for this test were poured.

To prevent downward migration and possible escape of concrete decomposition gases during the course of the experiment, the electrode penetrations through the bottom support plate were sealed using O-rings. As described in the next section, the test section was leak checked at 83 kPa differential pressure as part of pretest operations to verify a low leak rate. On this basis, essentially all concrete decomposition gases migrated upwards through the melt pool during the experiment, as opposed to partial loss through the bottom support plate of the apparatus. Reinforcing rod was eliminated so that it did not mask or delay attainment of a fully oxidized melt. The density of the siliceous concrete for this test was ~ 2341 kg/m^3, which was calculated based on the measured mass and volume of the CCI-6 concrete archive sample.

Table 2-4. Engineering Composition of CCI-6 Siliceous Concrete.

Constituent	wt %	Size Distribution
Aggregate	47.4	5-8 mm: 16.6 wt % 8-11 mm: 20.4 wt% 11-16 mm: 10.4 wt%
Sand	30.6	0-2 mm: 12.2 wt % 2-4 mm: 18.4 wt %
Type 1 Cement	15.3	N/A
Tap Water	6.7	N/A

Table 2-5. Chemical Composition of Siliceous Concrete.

Oxide	Wt%
SiO_2	53.65
Al_2O_3	4.03
Fe_2O_3	1.30
CaO	22.42
MgO	0.90
SO_3	0.77
Na_2O	0.67
K_20	0.97
TiO_2	0.15
P_2O_5	0.07
Mn_2O_3	0.07
SrO	0.04
CO_2	8.74
H_2O, Free	2.87
H_2O, Bound	3.61
Total	100.26

[4]Chemical analysis carried out by the Construction Technologies Laboratories (CTL Group) in Skokie, Illinois.

3.0 RESULTS AND DISCUSSION

3.1 Summary of Test Operations

Unlike previous CCI tests, the operating procedure for CCI-6 called for early cavity flooding after ablation had been established. The specific criterion for initiation of flooding was that any combination of two different thermocouples located 2.5 cm within the concrete indicated arrival of the ablation front (see Table 1-1). The specific instruments that would be used to make this determination are shown in Table 2-1. When this criterion was met, the cavity would be flooded. Following completion of bulk cooling, the power supply operating mode would be switched from constant power at the initial level of 210 kW (see Table 1-1), to constant voltage. Thus, if significant debris quenching occurred, power supply operation in this mode would approximately maintain *the specific power density in the remaining melt constant at the level established prior to cavity flooding* (see Appendix B in Reference [2] for a description of the theory behind the constant voltage operating scheme). The test would operate in this manner until the axial ablation depth reached 22.5 cm. If the lateral ablation reached 24 cm, then the backup UO_2 pellet and U_3O_8 powder liner and MgO sidewalls would terminate sidewall ablation and allow axial ablation to progress further. The crust lance would be used to break the crust at the melt water interface to provide data on *in-situ* crust strength, as well as information on the nature and extent of cooling after the crust was breached.

If the melt quenched and stabilized during the early flooding stage, then the test would be terminated. However, if the 22.5 cm ablation depth was reached, the water injection system would be reconfigured to inject water from below under a static water head of ~ 10 kPa as the nozzles gradually opened. As ablation progressed and nozzles opened to inject water, makeup to the header tank would be provided automatically by a supply line with a float switch that maintained the head in the range of 10±0.1 kPad. Additional water would only be added from the top at this stage if the test section plenum temperature started to rise above saturation, indicating that the top coolant layer had been evaporated. Past this point, the melt would either quench, or axial ablation would proceed to 32.5 cm. In either case, the experiment would be terminated by turning off the power supply that provides DEH to the melt.

CCI-6 was carried out on 18 March 2010. The event sequence is provided in Table 3-1. Time t = 0 corresponds to melt contact with the concrete basemat. The criterion used to define the onset of concrete ablation at a given location was that the local temperature reached the siliceous concrete liquidus of 1250 °C [15].

The test was initiated by applying power to the nichrome wire/sparkler located at the top of the powder charge at -0.8 minutes. Based on video camera data from the test section and plenum gas temperature readings, thermite ignition occurred at -0.6 minutes. Based on readings from the Type K thermocouples cast flush with the concrete basemat surface, the burn front reached the bottom of the powder bed and contacted the concrete in ~ 40 seconds (i.e., at 0.0 minutes), which was within the planning basis for the experiment. Peak melt temperatures near the center of the test section over the first minute of the interaction reached 2100 °C.

Table 3-1. CCI-6 Event Sequence.

Time (Min)	Event
-6.64	Data acquisition initiated.
-0.8	Power applied to thermite igniter wire.
-0.6	Thermite burn initiated
0.0	Thermite burn completed (burn time ~ 40 seconds); melt temperature ~2100 °C.
0.17	Main steamline fails at test section Tee leading to high temperature gas jet into cell. Gas discharged into the cell over the balance of the test.
0.66	No. 4 filter inserted; view reveals that plenum is dense with aerosols; churning melt conditions are evident.
0.71	Cavity flooded (to reduce temperature of gas jet into cell). Initially, the heat transfer rate to water is so intense that the water is boiled off as soon as it is added. Peak melt-water heat flux reaches 5 MW/m^2 and then steadily declines.
1.45	Continued water addition finally clears aerosols from plenum. View shows melt surface partially covered by crust that is floating on top of melt. Multiple eruptions occur through crust material. Water rapidly boiled away.
2.04-2.31	Surface dries out, revealing floating crust. Additional water was added, followed by eruptions at various locations on surface. Eruptions move around almost continuously on surface; site density is ~ 20 $holes/m^2$.
2.3	DEH input power reaches 210 kW but not held; conditions are unstable.
3.1	Melt surface eventually goes dark, indicating stable crust formation. Intense boiling off the surface of the crust. Occasional small eruptions lasting a second or two occur randomly around the surface of the crust.
4.14-7.29	Large scale eruptions begin in northwest corner of test section and these occur almost continuously until they stop at 7.29 minutes.
7.29-21.1	No sustained eruptions occur, and the debris-water heat flux steadily declines from ~ 500 kW/m^2 to ~350 kW/m^2 over the interval.
5.8-20.8	Power brought back to 210 kW, but current limit of 9000 Amps is also reached. During the period operations were maintained at the 9000 Amp limit, while power gradually drifted down to 190 kW.
9.57-39.4	Onset of axial basemat ablation at centerline and in all four quadrants; ablation rate remains slow during the balance of the test at ~ 2 cm/hour.
20.9-26.0	Onset of rapid ablation transient in south wall as the 2.5 cm erosion depth is reached at the +12.5 cm elevation at 20.9 minutes. Ablation rate averages 2.7 cm/min over this time interval as the ablation depth proceeds to 16 cm and then slows dramatically. North wall ablation is minimal.
22.9	2.5 cm erosion depth reached at the 0.0 cm elevation in the south wall.
21.1-25.9	Large melt eruptive events occur over the interval that result in a significant increase in upwards heat transfer rate. Eruptions start near the center of the south concrete wall at 21.1 minutes. The eruptions proceed at this location almost continuously until 23.2 minutes. Then the crust surface remains dark until 24.5 minutes. At this time, a large eruption event is initiated in the northeast corner of the test section, and proceeds almost continuously until ending at 25.9 minutes; the heat flux peaks at 3 MW/m^2 at 25.3 minutes. The crust surface goes dark again and remains that way for the rest of the test.
22.2	Operator is able to increase power back to target level of 210 kW due to increase in melt resistance; constant voltage operation begins at 27 volts.
24.6	Power supply operations switched from current to voltage control mode.
22.2-26.5	Input power falls steadily at constant voltage from 210 to 65 kW; at the end of the period the rate of power decrease slowed dramatically.
27.2	Ablation depth reaches 13 cm in south wall at 0.0 cm elevation before stabilizing
60.3-66.7	Crust lance inserted; modest load encountered until ~ 1.3 cm elevation is reached. Cooling transient observed on video *after* the lance is withdrawn.
26.5-150.9	Power gradually falls from 65 kW to zero at constant voltage. Power supply operations terminated at 150.9 minutes.
170.8	Data logging terminated.

Soon after the burn was completed (i.e. at 0.17 minutes), a hole was melted through the main steamline at the piping Tee directly on top of the test section, leading to a high temperature gas jet discharging into the cell. A substantial fraction of the gas products generated from the test leaked through this hole directly into the cell atmosphere over the balance of the test. Posttest examinations would reveal that this occurred due to the fact that high temperature melt was entrained into the steam line, and the subsequent melt impingement heat transfer at the Tee caused local melt through of the pipe. Despite this occurrence, experiment operations moved forward. At 0.66 minutes, a No. 4 filter was inserted on the lid video camera which revealed that a fairly robust core-concrete interaction was underway. The high temperature gas jet was focused upwards and appeared to be impinging upon the crane trolley that was positioned over the test section for later use when the crust lance would be lowered to breach the crust. On this basis, the operators flooded the cavity at 0.71 minutes to reduce the temperature of the gas jet issuing into the cell, as opposed to waiting for onset of ablation at the 2.5 cm depth at two concrete locations as the planned operating procedure dictated. The water system operator periodically added water to the test section for the balance of the experiment.

The initial heat transfer rate to water was so intense that the water is boiled off about as rapidly as it was added. The peak melt-water heat flux reached 5 MW/m^2 and then steadily declined. By 1.45 minutes, continued water addition finally cleared the aerosols in the plenum to the point that the debris surface could be clearly seen. The view indicated that the melt surface was partially covered by crust that was floating on top of melt. Multiple eruptions occurred through crust material. Water continued to boil aggressively, and the surface dried out from 2.04 to 2.31 minutes. This enhanced view showed that the crust segments were not bonded; rather, the structure fluctuated with the melt turbulence. More water was added during this interval; eruptions occurred following addition. Eruption sites seemed to move continuously around the surface; site densities were of the order of 20 holes/m^2.

DEH input power and operating voltage over the course of the experiment are shown in Figures 3-1 and 3-2. As the data indicate, by 2.3 minutes the operator was able to raise the DEH input power to the target level of 210 kW, but that level could not be held as the conditions were unstable. By 3.1 minutes, the surface of the crust eventually went dark, indicating stable crust formation. Intense boiling off the surface was observed. Occasional small eruptions lasting a second or two occurred randomly around the surface of the crust. At 4.14 minutes, large scale eruptions began in the northwest corner of the test section and these occurred almost continuously until stopping at 7.29 minutes. From 7.29 to 21.1 minutes, no sustained eruptions occurred, and the debris-water heat flux steadily declined from ~ 500 kW/m^2 to ~350 kW/m^2.

Over the time interval from 5.8 to 20.8 minutes, the input power was initially brought back to the 210 kW level, but the current limit of 9000 Amps was also reached. As a result, the operator held the current at the 9000 Amp limit, while power gradually drifted down to 190 kW. From 9.57 to 39.4 minutes, onset of axial ablation was detected at the basemat centerline and in all four quadrants. Axial ablation rate remained slow but steady during the balance of the test.

At 20.9 minutes, a rapid ablation transient was initiated in the south wall of the test section when the 2.5 cm erosion depth was reached at the +12.5 cm elevation. Over the next five minutes, the south wall ablation rate averaged 2.7 cm/min as the ablation progressed to 16 cm, and then slowed dramatically. Ablation of the north wall was minimal during this time.

Concurrent with the sidewall ablation burst, large melt eruptive events were observed that resulted in a significant increase in the upwards heat transfer rate. The eruptions started near the center of the south concrete wall at 21.1 minutes and proceeded virtually unabated until 23.2 minutes. The crust surface then went dark until 24.5 minutes. At this time, a large eruption event was initiated in the northeast corner of the test section that proceeded almost continuously until 25.9 minutes; the heat flux peaked at 3 MW/m^2 during this period at 25.3 minutes. The crust surface then went dark again and remained that way for the rest of the test.

The loss of electrical conductor from the melt zone due to the eruptions caused the effective resistance of the melt to increase. As a result, the electrical current requirement dropped and at 22.2 minutes the power was raised back up to 210 kW. Constant voltage operation began at this time at 27 volts. Due to the current limit, the average input power to the melt from time t = 0 until constant voltage operation was initiated at 22.2 minutes was 178 kW, which was ~ 15 % below target power of 210 kW. At 24.6 minutes, power supply operations were switched from current to voltage control mode to make this procedure simpler. Once constant voltage operation was initiated, input power fell steadily from 210 to 65 kW at 26.5 minutes; at the end of this period the rate of power decrease slowed dramatically. Past this point, power supply operation continued at constant voltage, and the input power declined slowly.

From 60.3 to 66.7 minutes, the crust lance was inserted to provide information about the debris profile and crust strength. Only a modest load was encountered until the probe tip reached ~ 1.3 cm elevation above the initial concrete surface elevation. A significant cooling transient occurred, but only after the lance was withdrawn. The video indicated that water was flooding into a hole made in the debris by the lance after withdrawal. From 26.5 to 150.9 minutes, the power gradually fell from 65 kW to zero at constant voltage. Power supply operations were terminated at 150.9 minutes. Data logging was subsequently terminated at 170.8 minutes.

3.2 Thermalhydraulic Results

Key thermalhydraulic results from the experiment included melt temperatures, lateral and axial concrete erosion rates, information on crust strength and morphology provided by the crust lance, and finally the debris water heat flux. This information is summarized below; full details are provided in [2]. The ramifications of these results are discussed later in this section.

Data from the melt temperature thermocouple array located near the basemat centerline is provided in Figure 3-3, while data from the two sidewall arrays are shown in Figures 3-4 and 3-5. To provide an indication of the overall melt temperature behavior during the test, a graph showing data from all thermocouples that saw melt conditions is provided in Figure 3-6. To improve readability, the data have been averaged over ~30 second (i.e., 6 point) intervals, and only data preceding the first off-scale reading by the units are shown. Past the first off-scale reading, the junctions are assumed to have failed, and thus the data are not deemed to be reliable.

These data indicate that the peak melt temperature following the thermite reaction was ~ 2100˚C. From the start of the experiment until onset of the rapid ablation burst in the south wall at ~ 21 minutes, melt temperatures declined steadily to an average of ~ 1900˚C. The solidus temperature for the initial corium composition was estimated as ~ 1880˚C [2]. Thus, the temperature response data shown in Figures 3-4 and 3-5 seems to indicate the sustained presence

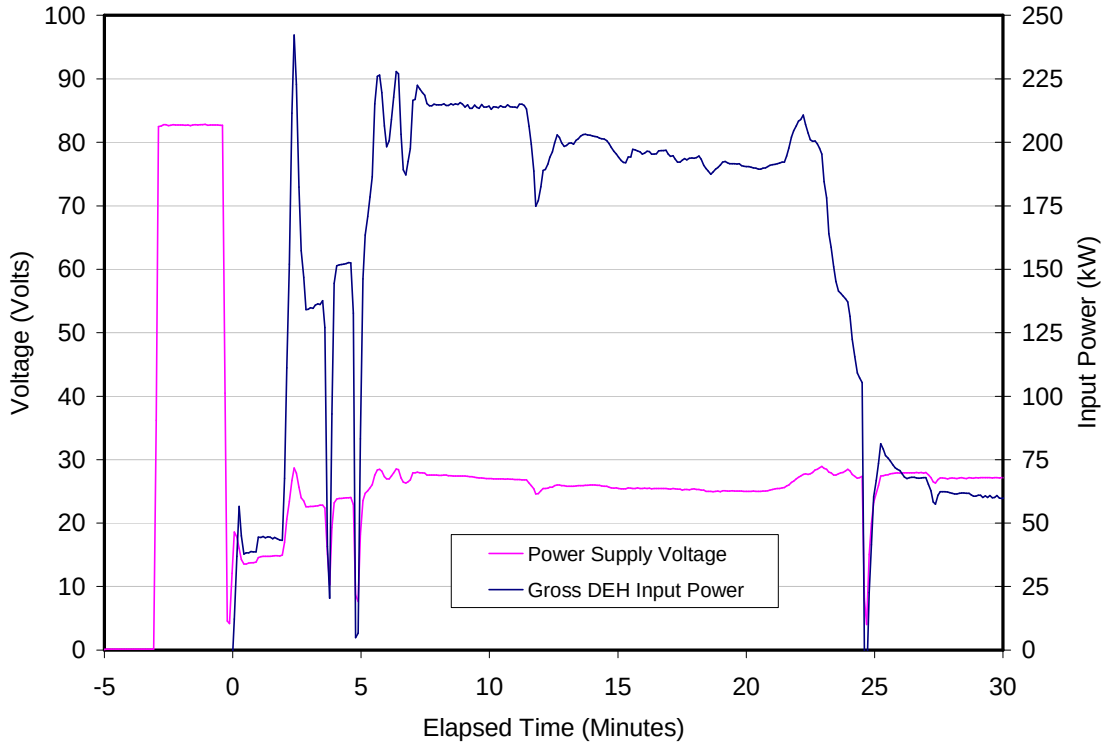

Figure 3-1. Power Supply Voltage and Power: Early Phase of the Test.

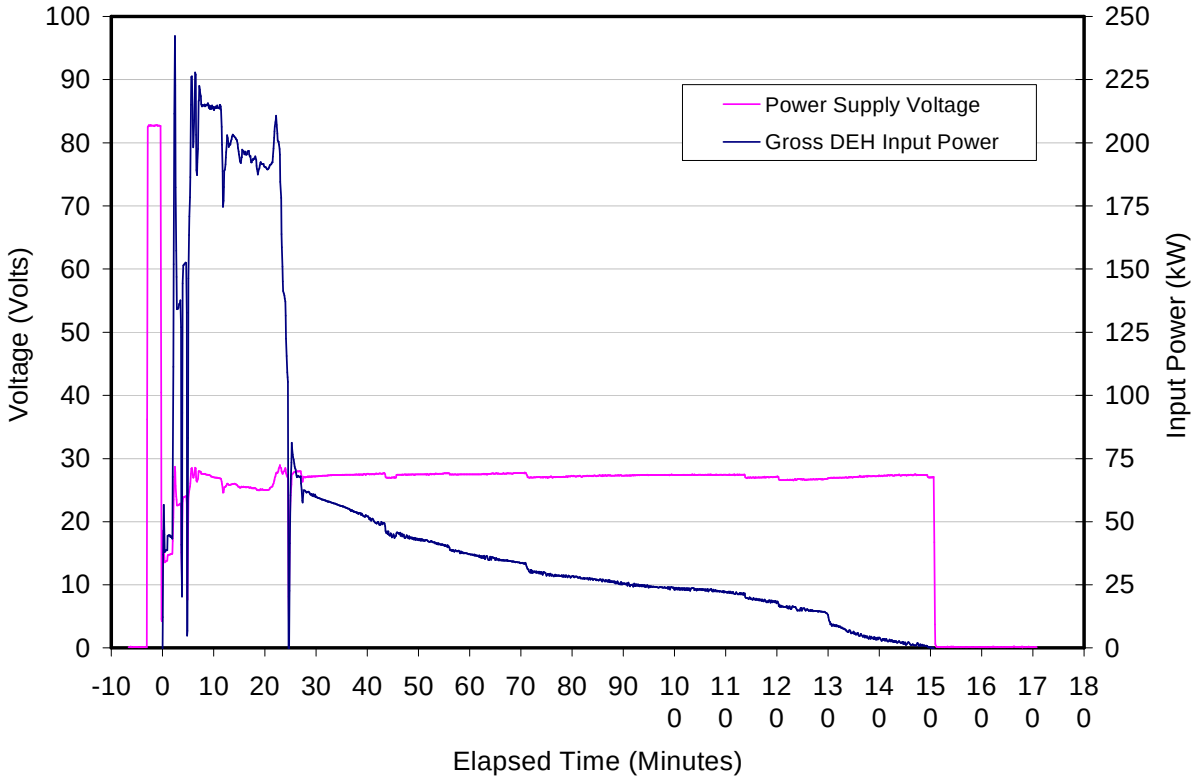

Figure 3-2. Power Supply Voltage and Power over the Entire Test.

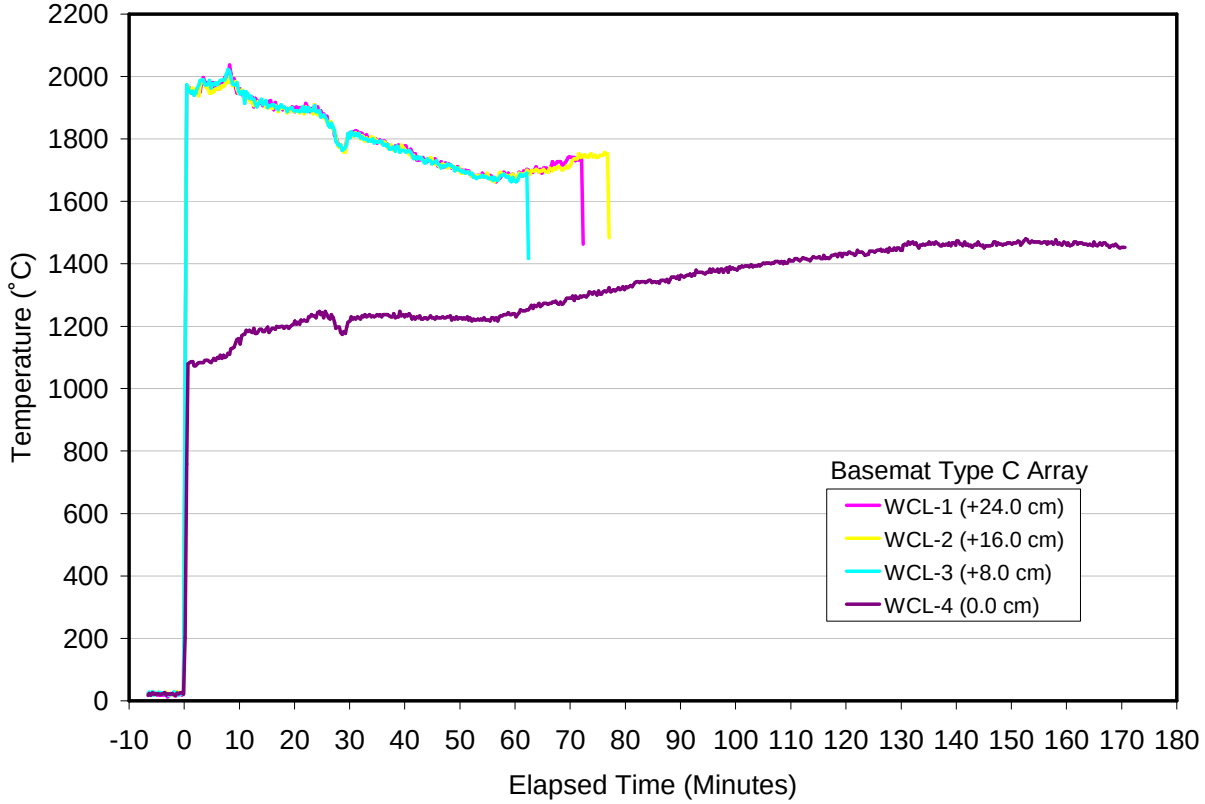

Figure 3-3. Melt Temperature Data from Basemat Type C "WCL" Array.

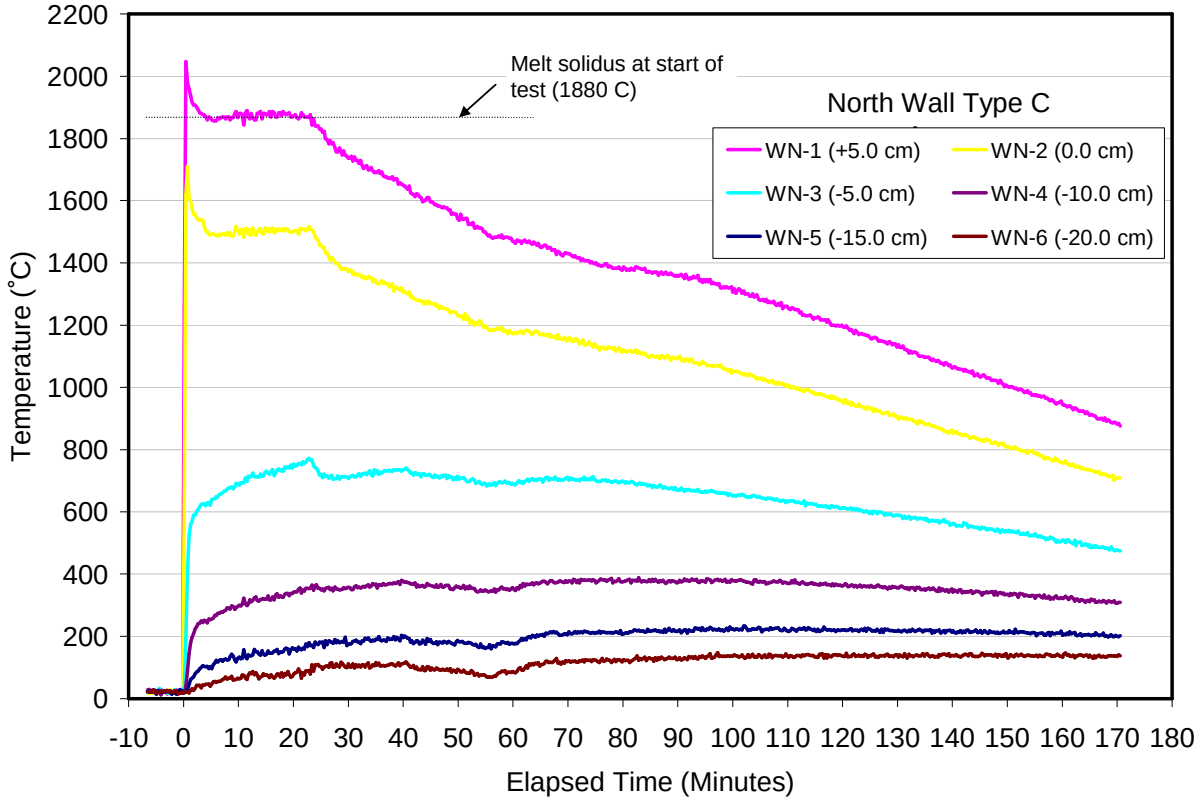

Figure 3-4. Melt Temperature Data from North Side Wall Type C "WN" Array.

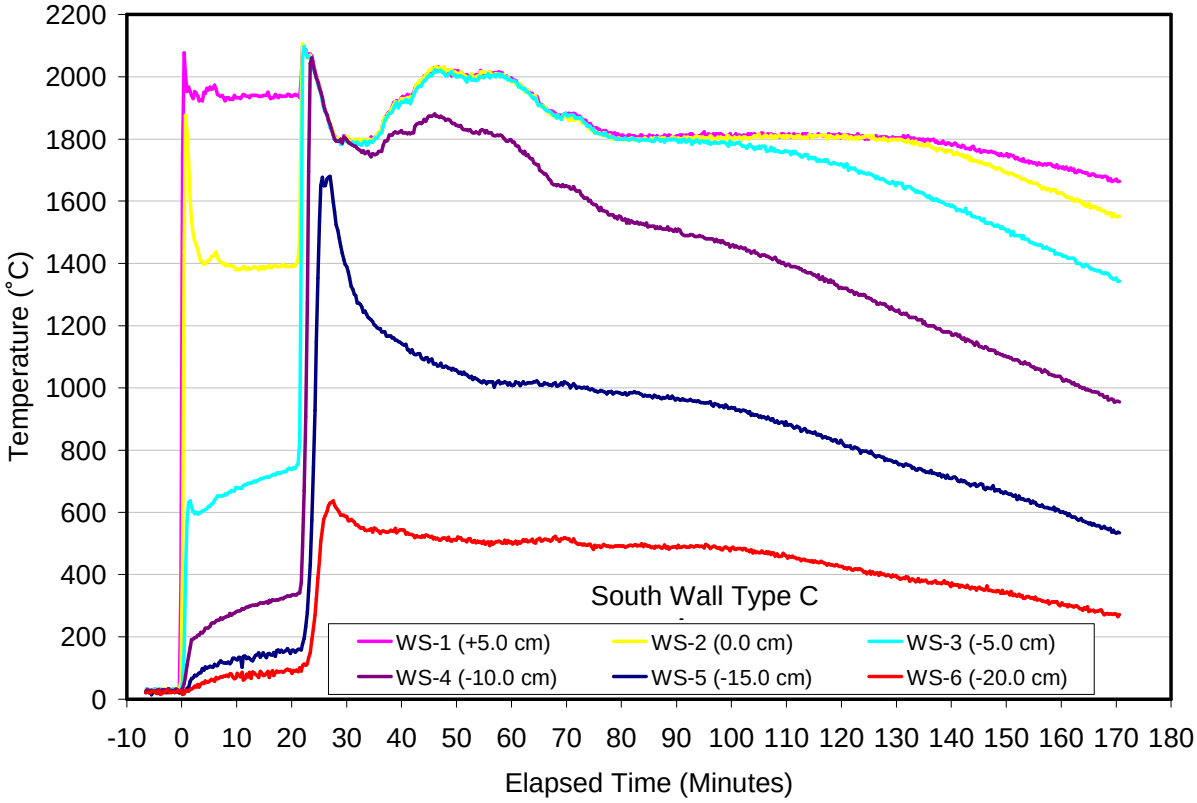

Figure 3-5. Melt Temperature Data from South Side Wall Type C "WS" Array.

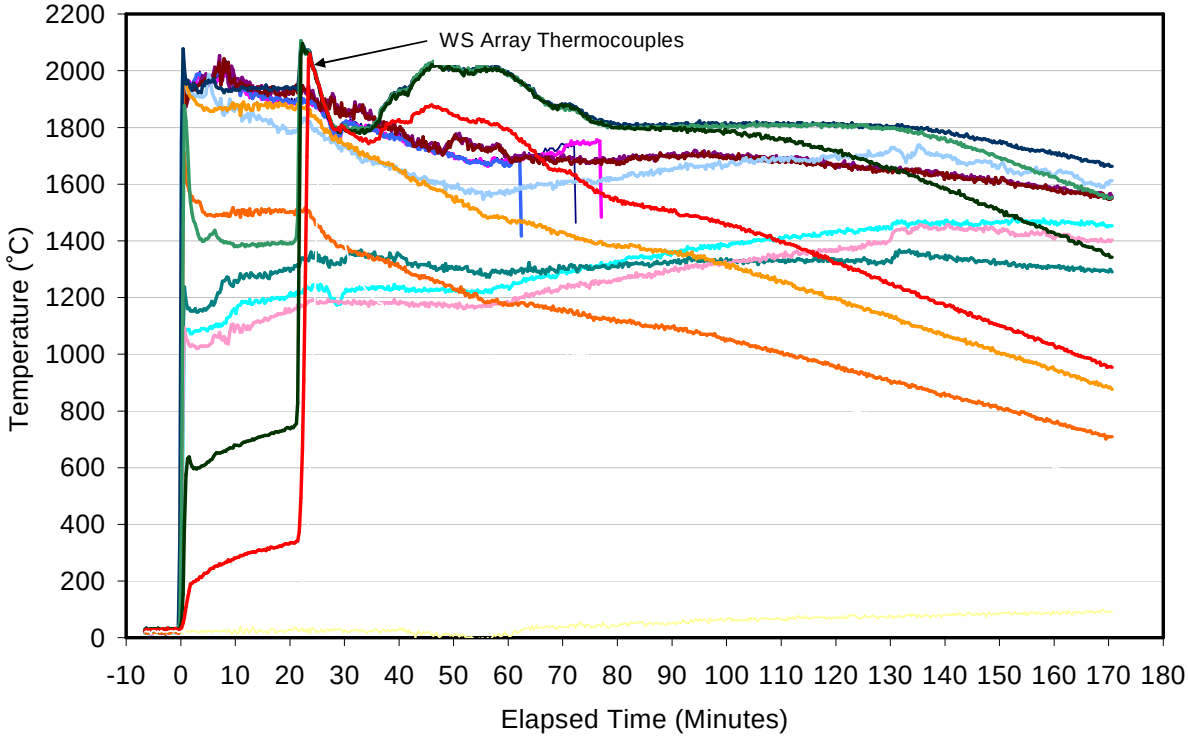

Figure 3-6. Data from all Melt Temperature Thermocouples.

of crust material near the north and south walls up to 21 minutes. However, shortly after 21 minutes the temperatures near the south wall rapidly increased to ~ 2100˚C, which is coincidentwith the onset of rapid ablation in this wall. The temperature escalation is thusconsistent with the sudden loss or failure of a crust that was protecting this surface. Over the next six minutes, the temperatures near the south wall drop steadily until they plateaued at ~ 27 minutes at a level of 1800˚C; see Figure 3-7. This plateau occurs at about the same time as the ablation transient in the south wall terminated (see Table 3-1). The data in Figures 3-5 through 3-7 suggest that the sensible energy for ablation during the transient was provided by the melt fairly close to the south wall. This observation can be checked using data from the posttest examinations, which revealed that the ablation in the south wall totaled about 13 l in volume, or ~ 31 kg given the concrete density of ~ 2370 kg/m^3 (see Section 2.4). Assuming a concrete decomposition enthalpy of ~ 2 MJ/kg, then the energy required to ablate the 31 kg of material would be ~ 62 MJ. Further assuming a corium specific heat of ~ 600 J/kg-K along with the fact that the local melt temperature drop during the transient was ~ 300˚C then an energy balance reveals that the melt mass that participated in the transient was ~ 340 kg. This amounts to ~ 1/3 the initial melt mass used in the experiment. Thus, the concept that the ablation transient was localized and involved only a fraction of the overall melt pool seems plausible. Another possible explanation[5] for the transient is based on a cement paste liquefaction concept where the siliceous aggregate was only partially melted when the crust disappeared. This relatively cold material was then introduced into the melt pool once the crust failed, causing the temperature decrease. After the aggregate melted, the pool temperature was then able to rise again.

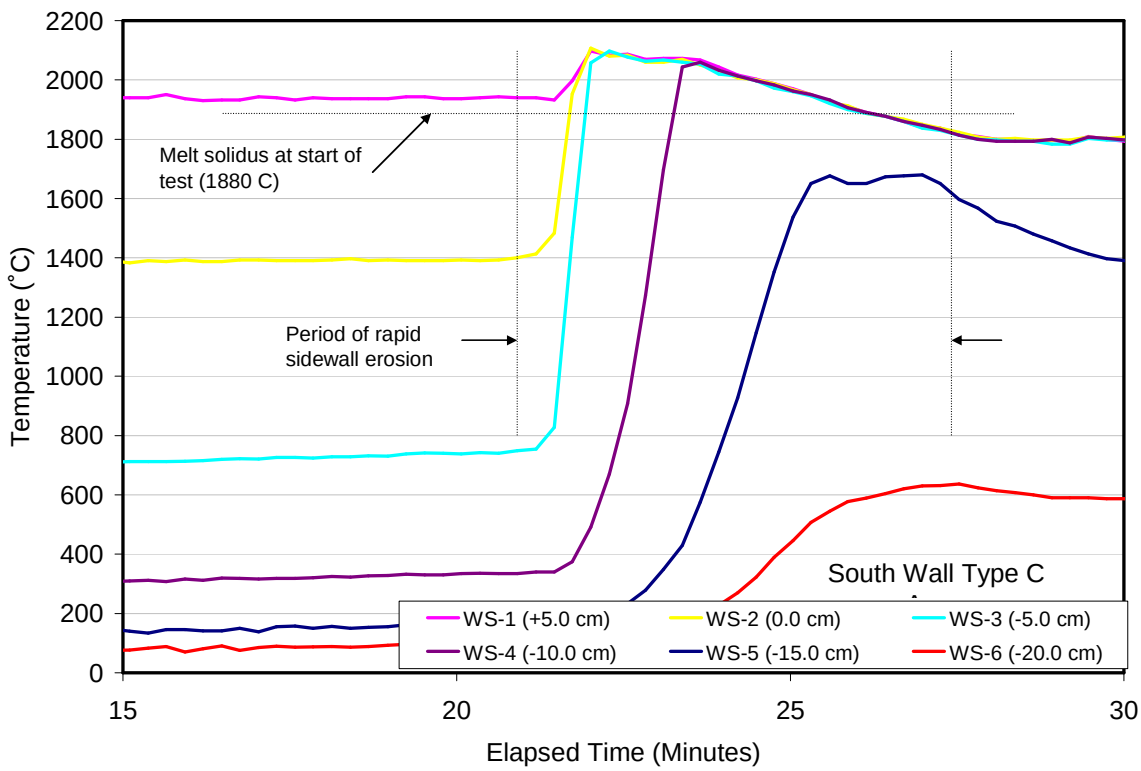

Figure 3-7. Melt Temperature Data from "WS" Array: Expanded Scale.

[5] M. Cranga and J.-M. Bonnet, IRSN, personal communication (e-mail) to M. T. Farmer, ANL, 28 September 2010.

Following the ablation transient, the data from the Type K arrays cast in the concrete (see discussion below) suggest that concrete ablation was minimal. Thus, gas sparging from concrete decomposition would also have been minimal. As is evident from Figure 3-6, the lack of bubble-induced convection within the melt resulted in large temperature gradients across the extent of the test section that ranged up to 500˚C or more. The disparity is enhanced by the fact that this test contained the lowest initial concrete content of any in the program (i.e., 6 wt %), and ablation was minimal so that substantial concrete was not added to the melt that would have lowered the freezing point. Thus, the melt would have been quite stiff and conduction within the debris would not have been negligible. Under these conditions, large temperature gradients can develop. By the end of the experiment, the temperatures varied from 700 to 1680˚C.

In terms of the cavity heatup and ablation behavior, the thermal response at the basemat centerline as the test progressed is shown in Figure 3-8, while the analogous data in the North and South concrete sidewalls at the +12.5 cm elevation are provided in Figures 3-9 and 3-10, respectively. As noted previously, only data preceding the first off-scale reading by the thermocouples are shown. When a thermocouple reached the siliceous concrete liquidus temperature of 1250 ºC [15], the melt was considered to be in contact with the thermocouple at the junction location. Based on this assumption, Figure 3-11 provides the axial ablation depth versus time based on the basemat Type K arrays, while Figure 3-12 provides the analogous radial ablation data in the South sidewall. As can be inferred from Figure 3-13, ablation in the North wall was minimal for this test. Finally, Figure 3-14 provides a comparison of the ablation depths versus time recorded on all three concrete surfaces.

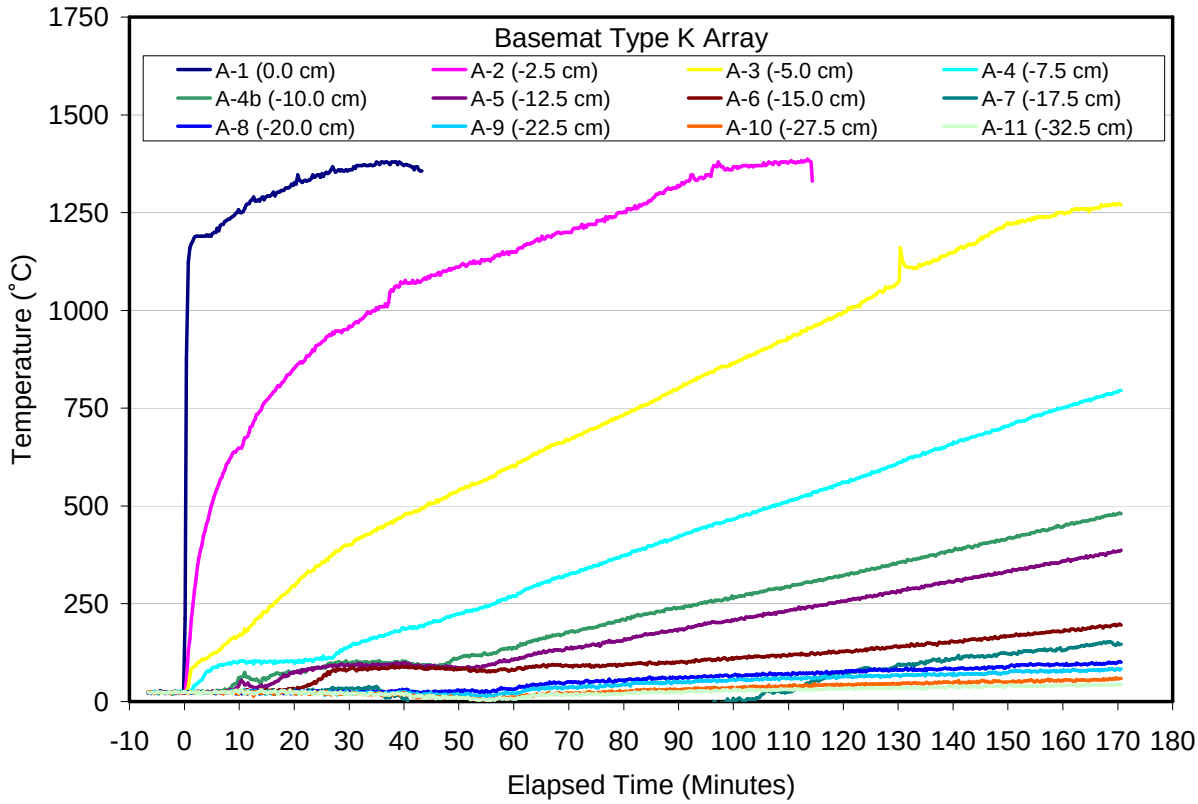

Figure 3-8. Thermal Response of the Concrete Basemat at the Centerline.

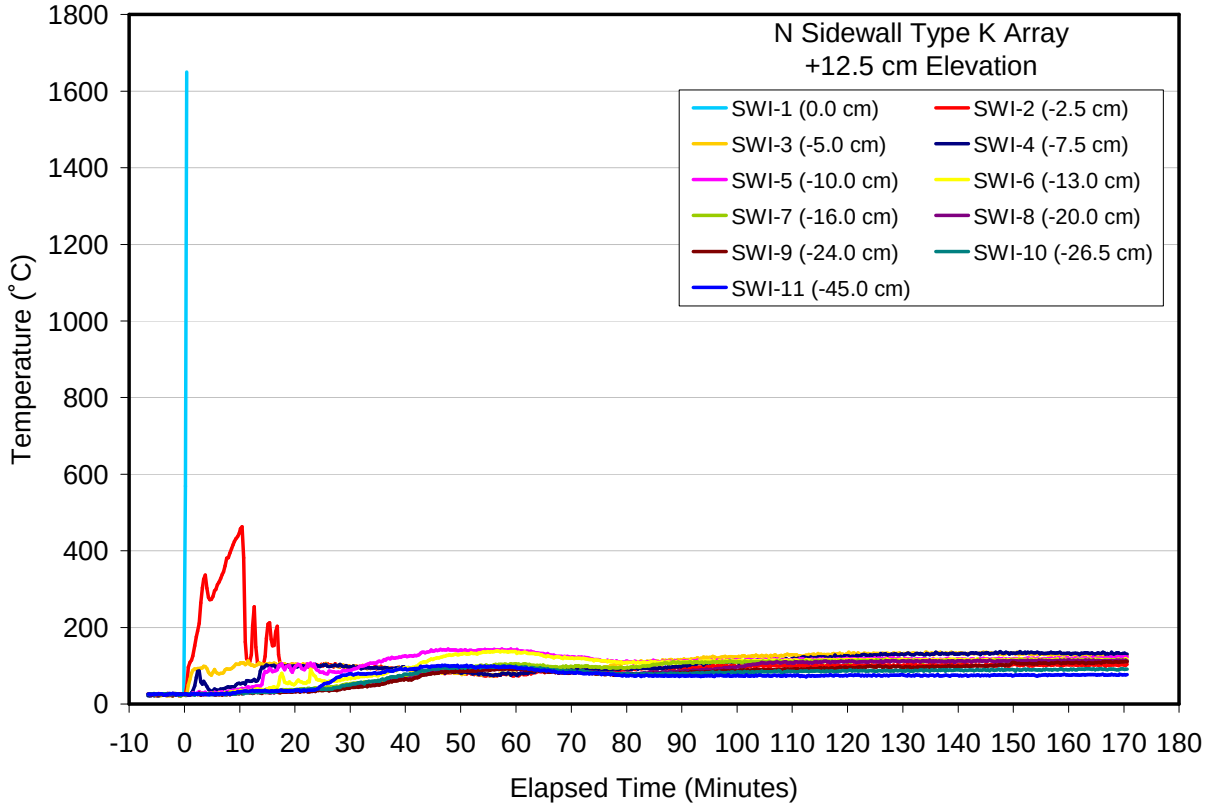

Figure 3-9. North Concrete Sidewall Thermal Response at +12.5 cm.

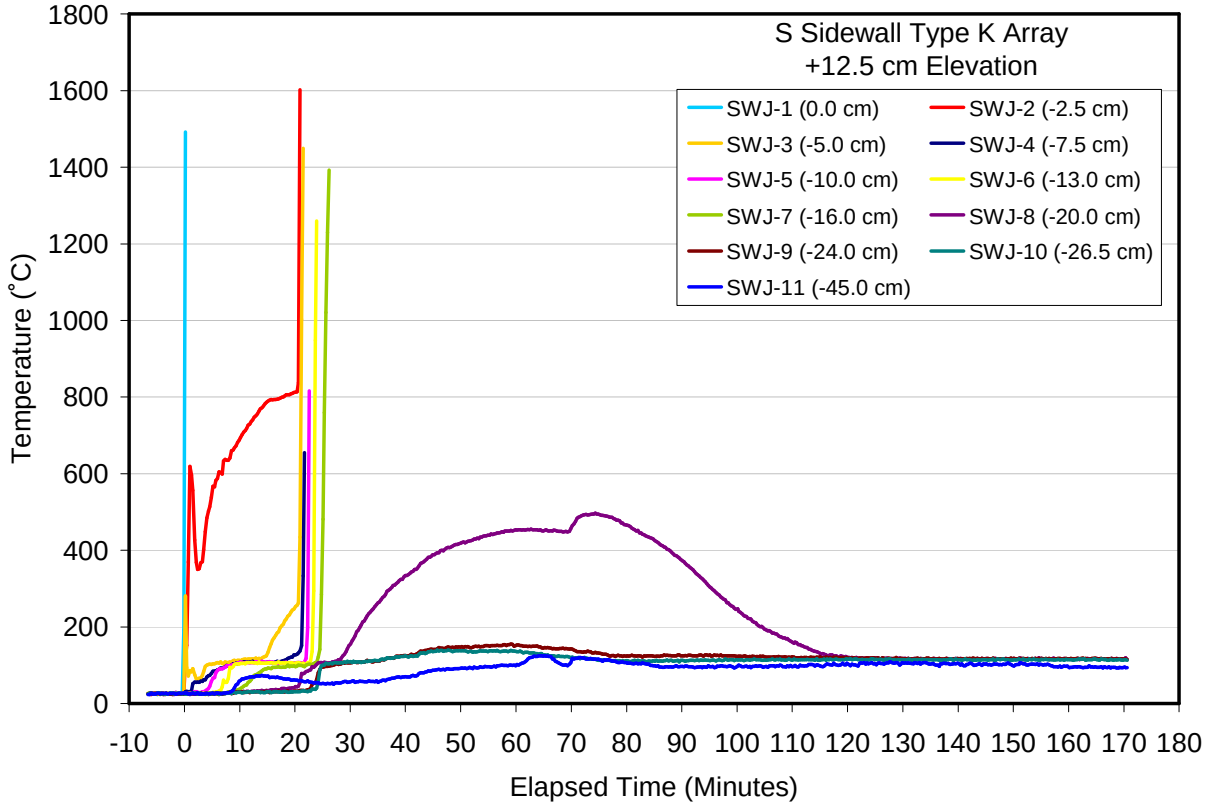

Figure 3-10. South Concrete Sidewall Thermal Response at +12.5 cm.

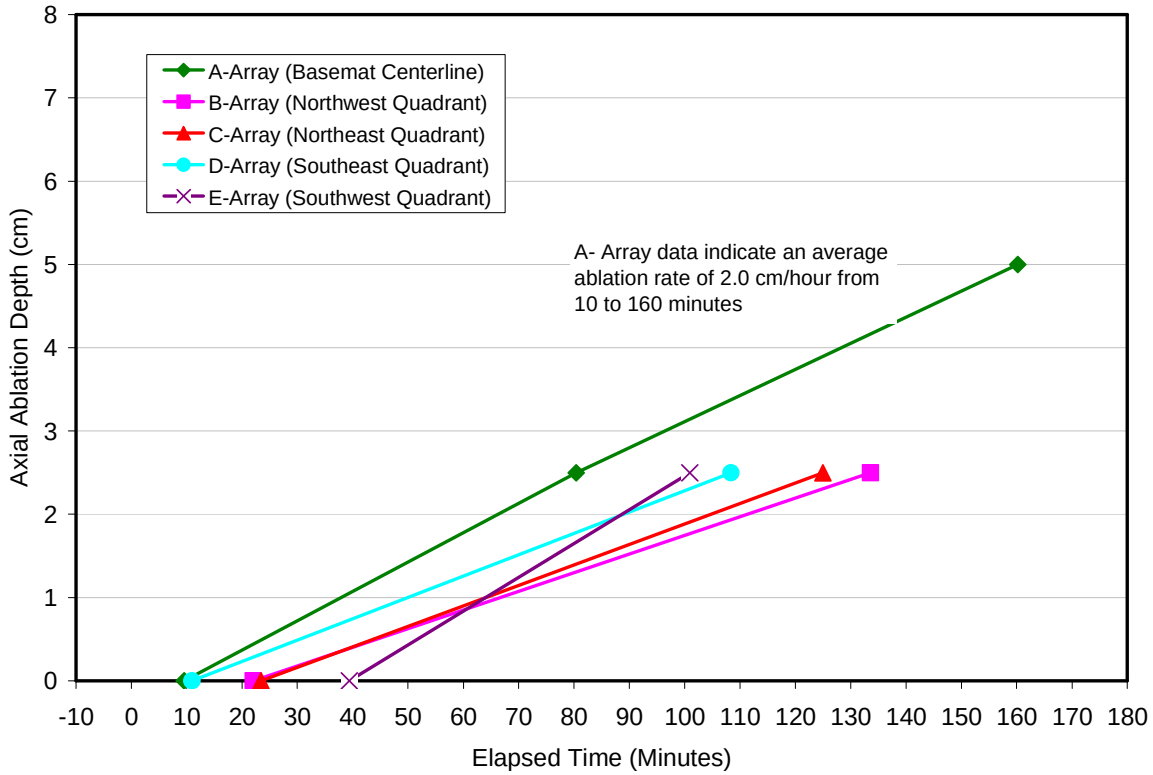

Figure 3-11. Basemat Axial Ablation Front Location.

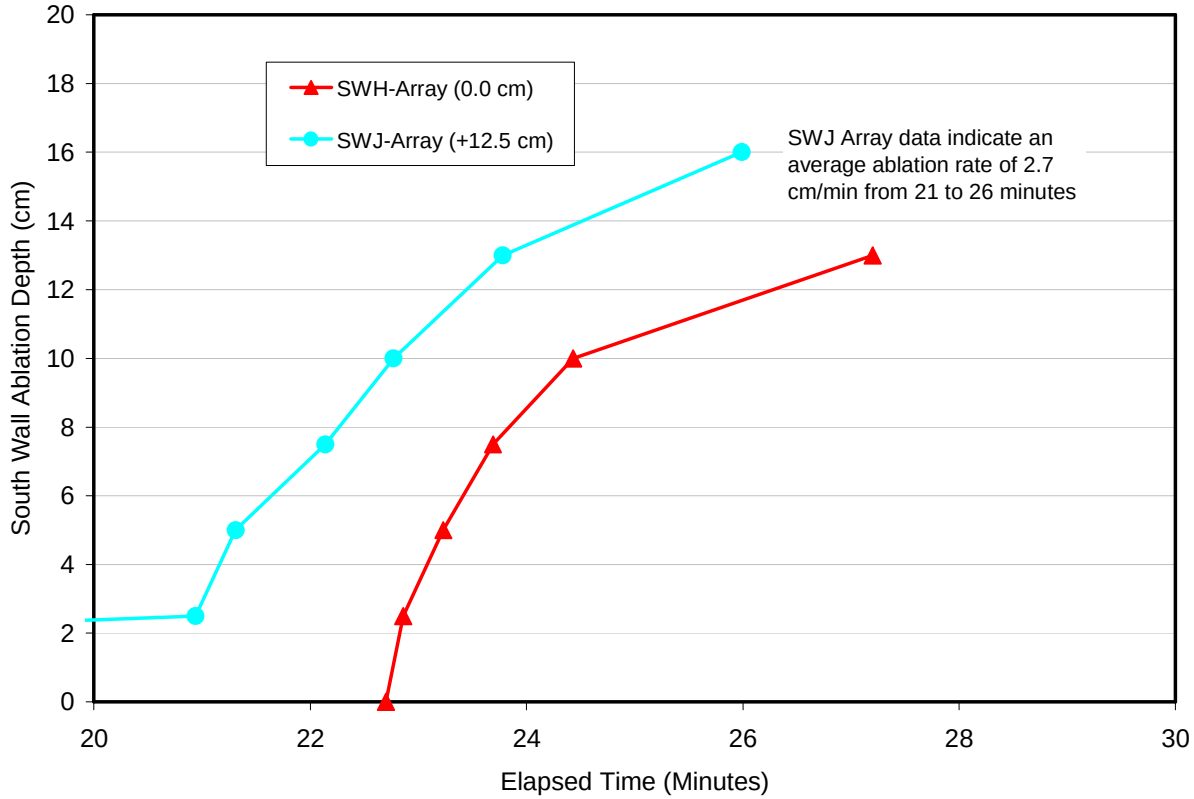

Figure 3-12. South Sidewall Radial Ablation Front Location.

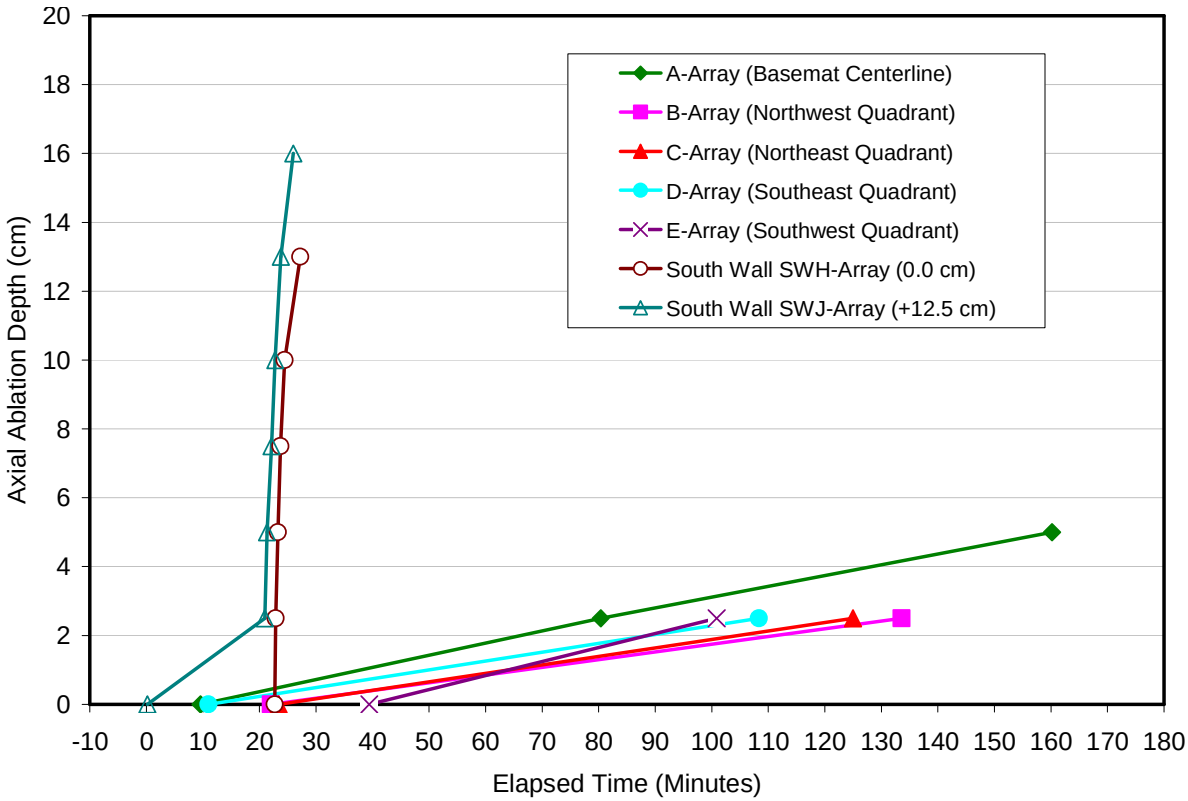

Figure 3-13. Comparison of Axial and Radial Ablation Depth Data versus Time.

Examination of these figures indicates that axial ablation proceeded relatively slowly but steadily at a rate of ~ 2 cm/hour over the course of the experiment. Conversely, the only significant sidewall ablation occurred in the south wall over the time interval from ~ 21 to ~ 27 minutes. During this interval, the ablation depth progressed to a depth of 16 cm, yielding an average ablation rate of ~ 2.7 cm/min. As is evident from Figure 3-10, water eventually infiltrated down the interface between the corium and the degraded concrete sublayer at this location (as well as the north wall), thereby terminating sidewall heatup and ablation. Vaporization of this infiltrating water could have enhanced the gas release through the melt and as a consequence the intensity of melt eruptions. Assuming a siliceous concrete decomposition enthalpy of 2 MJ/kg, then the local ablation rate of 2.7 cm/min observed on the south wall would require a convective heat transfer rate from the melt of ~ 2.1 MW/m^2. This intense heating rate is consistent with the rapid melt temperature drop observed near this wall when the ablation transient occurred, as discussed previously.

As shown in Table 3-1, the crust lance was inserted approximately an hour after cavity flooding to obtain data on the debris morphology and crust strength, as well as the enhancement in the debris cooling rate following a crust breach event. The outputs from the lance force and displacement transducers are shown concurrently in Figure 3-14. Also shown on the figure are the approximate elevations of key debris interfaces that were determined on the basis of the posttest examinations (see Section 3.3) as well as other test data. These interfaces include the top of a particle bed produced by melt eruptions; the interface between the bed and underlying

fractured crust; the top surface of the solidified melt pool; and finally the location of the concrete basemat surface at the time the lance was inserted (as inferred from Figure 3-11).

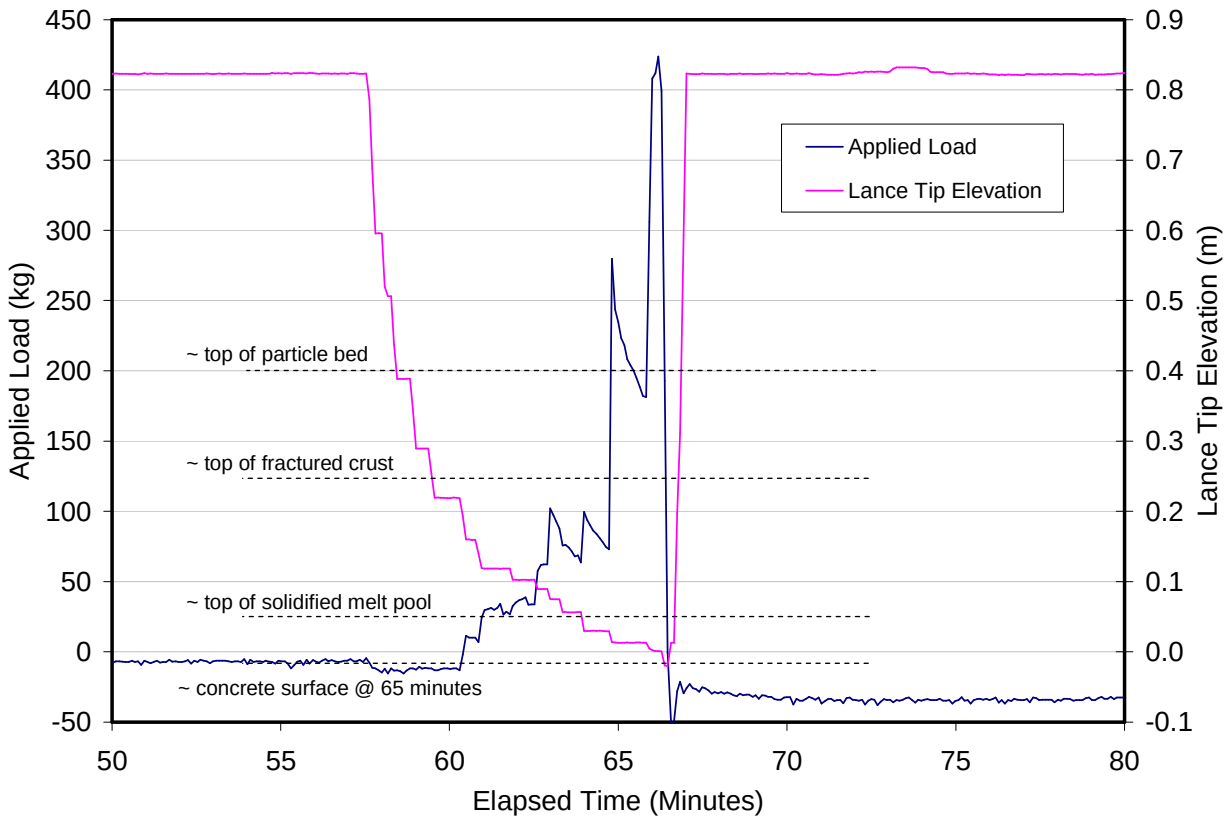

Figure 3-14. Crust Lance Applied Load and Position vs. Time.

As the lance was inserted, no detectable load was measured until the tip had reached the 22 cm elevation over the initial concrete surface at 60.3 minutes. At this elevation, the tip was already 6 cm below the collapsed pool depth of 28 cm at the start of the test. The data further indicate that the lance had already penetrated through the ~ 18 cm deep particle bed by this time. The lack of a significant load indicates that the bed was loosely packed. The first load detection at the 22 cm elevation was most likely the top of the fractured crust, but the load was quite small (< 7 kg). On this basis, the lance was inserted further. The load continued to increase, but not in a step-function fashion as would be expected for a rigid structure. Rather, the load increased gradually, and load increases were followed by gradual relaxation periods as opposed to a rapid release of strength that again would be associated with the failure of a rigid structure. Posttest examinations indicated that in this range, the probe tip was passing through fractured crust material that could be removed by hand, and this explains the relatively low force required to penetrate the material. Finally, at 65.8 minutes when the probe tip was at the 1.3 cm elevation, the lance load increased to near capacity (i.e., 424 kg vs. the deadweight mass of 450 kg), and a brittle-type failure occurred. At this time in the experiment, the axial ablation depth was in the range of 1-2 cm (see Figure 4-15). Thus, the presence of the hard material at the 1.3 cm elevation would be consistent with a 2-3 cm thick crust over the concrete surface, and the measured load would be indicative of the failure of this crust as opposed to one formed at the melt-water interface.

During the insertion period, there was no detectable increase in the debris cooling rate (see discussion below). However, when the lance was removed the quench rate increased, and the lid video camera showed a weak image of a hole present in the crust with water flooding beneath. Thus, removal of the lance apparently made a hole for the water to infiltrate down into the rubble bed and further increase the debris cooling rate.

Other key test objectives for CCI-6 were to: i) obtain data on the nature and extent of the corium quench process under early cavity flooding conditions, and ii) obtain data on the extent of corium cooling by bottom water injection through porous concrete nozzles cast in the basemat. However, the latter objective could only be satisfied if the axial ablation depth proceeded to 27.5 cm. For this test, axial ablation was limited to ~ 5 cm and so data on the second (bottom water injection) cooling mechanism was not obtained as a part of this experiment.

Normally, all steam from the test section is condensed within the instrumented quench system tanks. The debris-water heat flux can then be readily deduced from the steam condensation rate in the quench tanks. However, meltthrough of the main steamline (see Table 3-1) meant that part of the steam was vented directly into the cell atmosphere, and other methods (instruments) had to be used to evaluate the overall steaming rate over the test. This method was straightforward but tedious; full details of the analysis are provided in [2]. The resultant debris-water heat flux calculated from the steaming rate by assuming a saturated coolant latent heat of vaporization at atmospheric pressure of 2.256 MJ/kg, as well as a planar corium surface area of 0.7 m x 0.7 m = 0.49 m^2, is shown in Figure 3-15. The DEH input power, normalized with the test section planar area, is also shown in the figure along with the times of key events such as melt eruptions and the lance insertion sequence (see Table 3-1).

The peak melt-water heat flux reached 5 MW/m^2 soon after initial cavity flooding and then steadily declined. During the initial interaction, the high cooling rate was partially attributable to melt eruptions that were observed over the first few minutes of the experiment. From 7.29 to 21.1 minutes, no sustained eruptions occurred, and during this phase the debris-water heat flux declined further from ~ 500 kW/m^2 to ~350 kW/m^2. Over the time interval from 21 to 27 minutes, multiple melt eruptions were observed that caused a transient increase in the heat flux up to a level of 3 MW/m^2. Following this event, the heat flux steadily declined from ~ 500 kW/m^2 to ~ 120 kW/m^2 at the time the crust lance was inserted at 60 minutes. Upon removal of the lance, another transient increase in the flux occurred up to a level of ~ 1 MW/m^2. The video data seemed to indicate that water was flooding into a hole made within the debris after the lance was withdrawn, and this water inflow resulted in the increase in the cooling rate. After the lance was removed, the heat flux declined and stabilized at an average value of ~ 100 kW/m^2 where it remained for the balance of the test.

The integrated energy removal to overlying water is compared with the integrated heat input from DEH in Figure 3-16. This data, as well as that shown in Figure 3-15, indicates that the debris-water cooling rate far exceeded heat input over the course of this test. This finding is consistent with the limited cavity erosion that occurred, and is further rationalized by the posttest debris morphology that indicated a large debris fraction that appeared to be quenched in a coolable debris configuration.

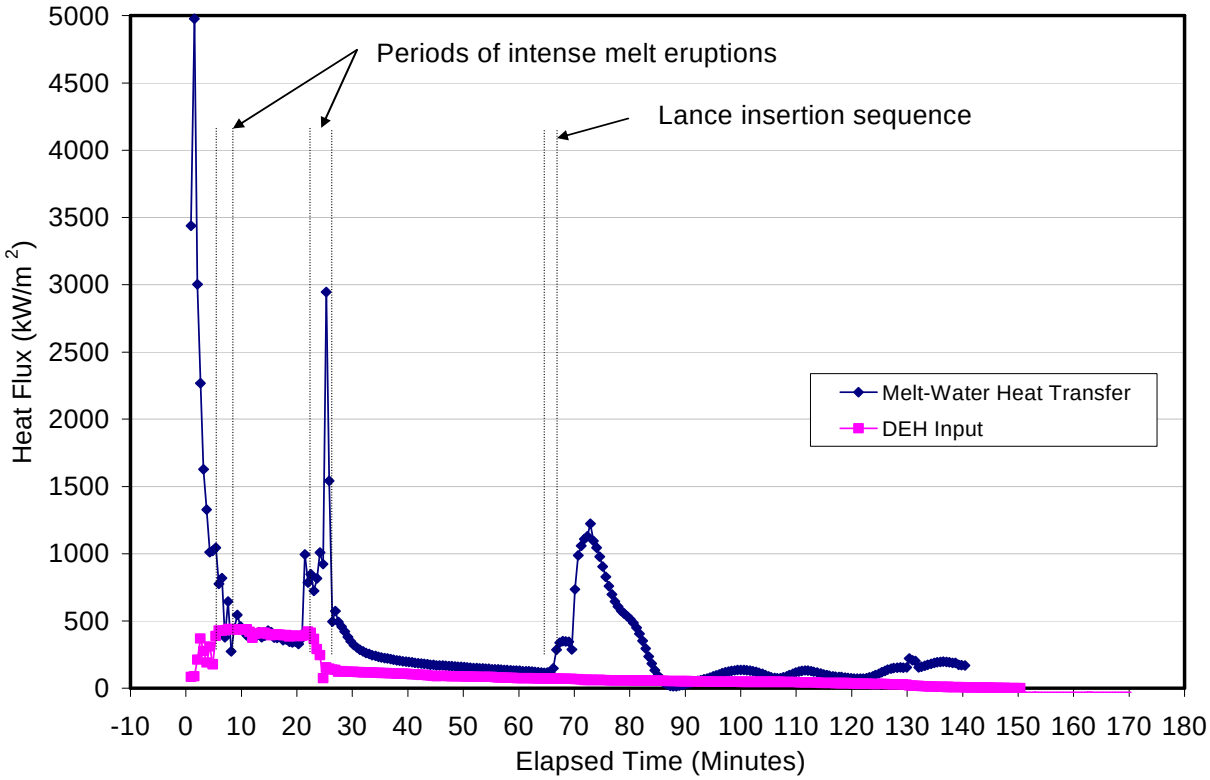

Figure 3-15. CCI-6 Debris-Water Heat Flux (Top Flooding).

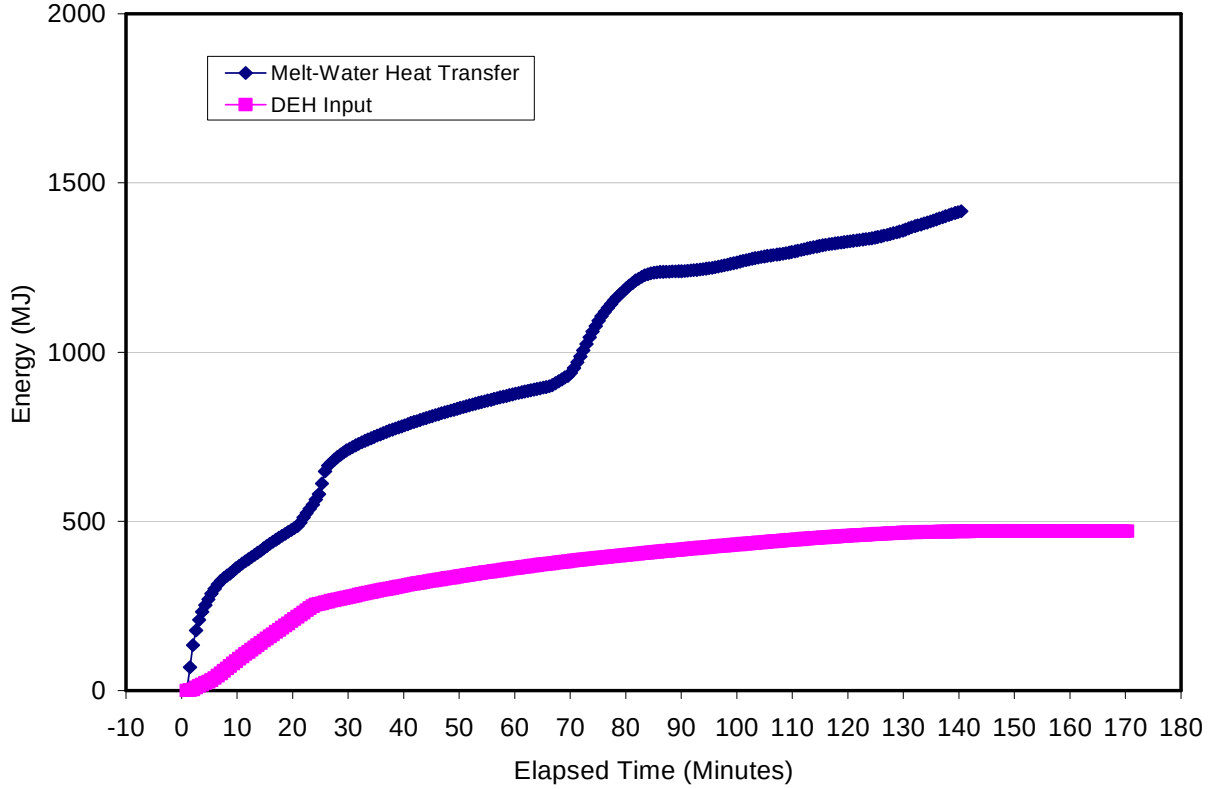

Figure 3-16. Integrated Heat Removal to Water and Heat Input to Melt from DEH.

3.3 Posttest Examination Results

Following the experiment, the apparatus was disassembled to document the posttest debris configuration. As a part of this effort, the steamline was examined in order to characterize the hole sizes that developed during the thermite burn. This information was needed to evaluate the fraction of steam lost through these holes during the test; details are provided in [2].

A photograph showing the top surface of the debris after removal of the test section lid, top, and middle sidewall sections is provided in Figure 3-17. The upper surface of the material was composed of a loose particle bed. After the bed surface elevation profile was measured, the bed was removed by hand and segregated for a separate weight measurement. A photograph of this material is provided in Figure 3-18. These efforts revealed the top of a crust layer that was quite fragile and could also be removed by hand. This procedure revealed the presence of two volcanic mounds. The first was located adjacent to the south wall, while the second was centered just north of the centerline of the debris. Photographs of these structures are provided in Figure 3-19. During removal of these mounds, an effort was made to try to characterize the 'vent holes' through this material, but this proved to be difficult. First, the material was quite porous and was filled with pores and holes that ranged from a few millimeters to a centimeter, and it was difficult to determine which of these holes actually served as vent sites during the test. Second, when one attempted to remove this material, it crumbled quite easily which made it even more difficult to trace any continuous pathway through the material. However, the volcano near the test section centerline had a large fold or crease that could have formed a pathway for melt eruptions (see Figure 3-19b). This opening was approximately 3 cm in width.

Figure 3-17. Top View of Particle Bed After Removal of Upper Sidewall Sections.

Figure 3-18. Closeup Photograph of Material Removed from Particle Bed Over Fractured Crust.

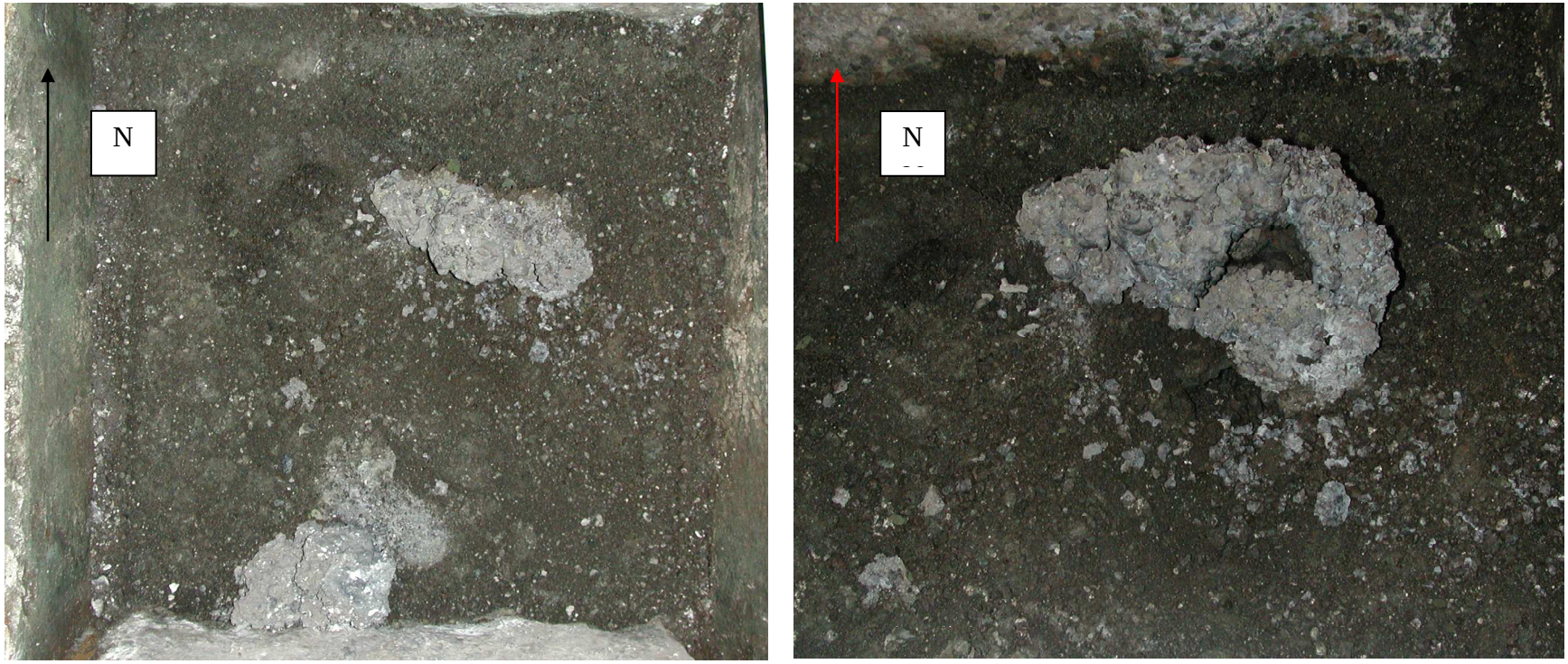

(a) **(b)**

Figure 3-19. Views of the Debris After Particle Bed Removal (a) from the Top and (b) Closeup of the Volcanic Mound in the North-Central Region of the Debris as Viewed from the South.

Once the crust surface characteristics and elevation profile were documented, disassembly moved forward by first removing the two inert MgO sidewalls and then the two concrete walls to reveal the corium remaining over the basemat. Face-on views of the two sidewalls after removal are shown in Figure 3-20, while photographs of the corium remaining over the basemat are provided in Figure 3-21. Further examinations confirmed the data recorded during the test; i.e., ablation of the north wall was minimal, while the peak ablation depth into the south wall was ~ 16 cm. Moreover, the crust material remaining over the basemat was also found to be quite fragile and porous, and this material could also be removed by hand. Thus, this fractured crust material was also recovered and segregated for weight determination; a photograph illustrating the material characteristics is provided in Figure 3-22. Although there were several large pockets of porosity found in this material (see Figure 3-21), this stage of disassembly did not reveal any large continuous caverns that separated the crust from the underlying melt pool, as occurred in the MACE tests [9]. On this basis, the test configuration appeared to achieve a floating, or at least non-separated, boundary condition that may well explain the exceptional cooling behavior that was observed.

During disassembly, the various debris regions were carefully segregated and weighed to better document the debris distribution. A drawing showing key features is provided in Figure 3-23. These measurements indicated that 186 kg of core melt was rendered in the form of a porous debris bed due to melt eruptions, which amounts to ~ 21 % of the initial melt mass. The mass of porous, fractured crust material that could be easily removed by hand amounted to 266 kg, which amounts to ~ 30 % of the initial mass. Thus, over ½ of the initial core melt inventory appears to have been quenched and rendered in a coolable debris configuration. The data also indicated that this most likely occurred over the first 30 minutes of the core-concrete interaction.

Further analysis of the posttest debris configuration indicates that ~ 87 kg of concrete was eroded during the test. Given the H_2O and CO_2 contents of the concrete (see Table 2-4), then this amount of material would liberate ~ 379 moles of gas upon decomposition, which is equivalent to a gas volume of ~ 9.3 m^3 at standard conditions, or ~ 71 m^3 at an assumed melt temperature of 2000˚C. Conversely, the 186 kg of erupted core melt corresponds to a liquid volume of ~ 28 liters (calculated density for CCI-6 initial melt composition is ~ 6560 kg/m^3). Thus, the melt entrainment coefficient (defined as erupted melt volume divided by total gas volume produced by core-concrete interaction at melt conditions) is calculated to be 0.04 % for CCI-6. As shown by Bonnet et al. [16], this entrainment coefficient is within the range of that which can achieve debris coolability on the basis of melt eruption cooling behavior alone during a prototypic ex-vessel core melt accident.

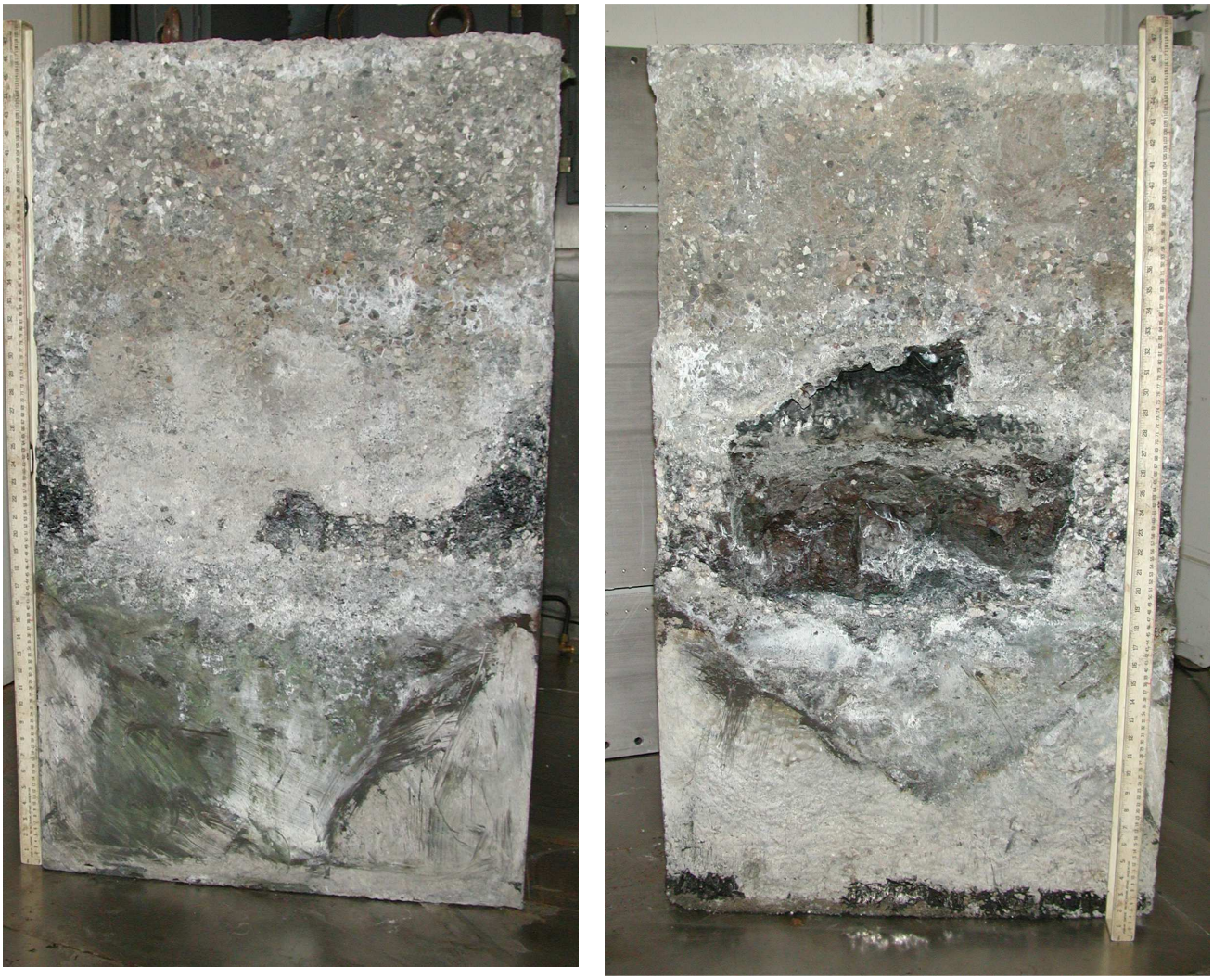

(a) **(b)**

Figure 3-20. Face-on Views of (a) North and (b) South Concrete Sidewalls After Removal.

3.4 Discussion

The objectives of CCI-6 were to: 1) carry out a large scale integral-effect test to provide data on core debris coolability under early *top flooding* conditions, and if the corium did not quench during this initial interaction, 2) provide additional data on coolability under *bottom flooding* conditions wherein water is injected into the melt through nozzles cast in the basemat. The overall experiment approach taken to meet these objectives was to: 1) enlarge the test section to minimize scaling distortions, and 2) incorporate an array of water injection nozzles into the core-concrete interaction test apparatus to inject water from below. Specifically, the test section was enlarged to incorporate a 70 cm x 70 cm basemat, and the initial melt depth was increased to 28 cm (900 kg melt mass). The thermite was redesigned to reduce the amount of concrete initially present (i.e., 6 wt %) to better mockup early cavity conditions. Water was intended to be added to the cavity as soon as ablation began. The basemat was redesigned to accommodate an array of water injection nozzles to quench the melt from below if the melt was not quenched earlier, and ablation proceeded to 27 cm.

(a) **(b)**

Figure 3-21. Views of Corium Debris Remaining Over the Basemat as Viewed from (a) North and (b) South.

Figure 3-22. Closeup Photograph of Fractured Crust Material after Removal from Test Section.

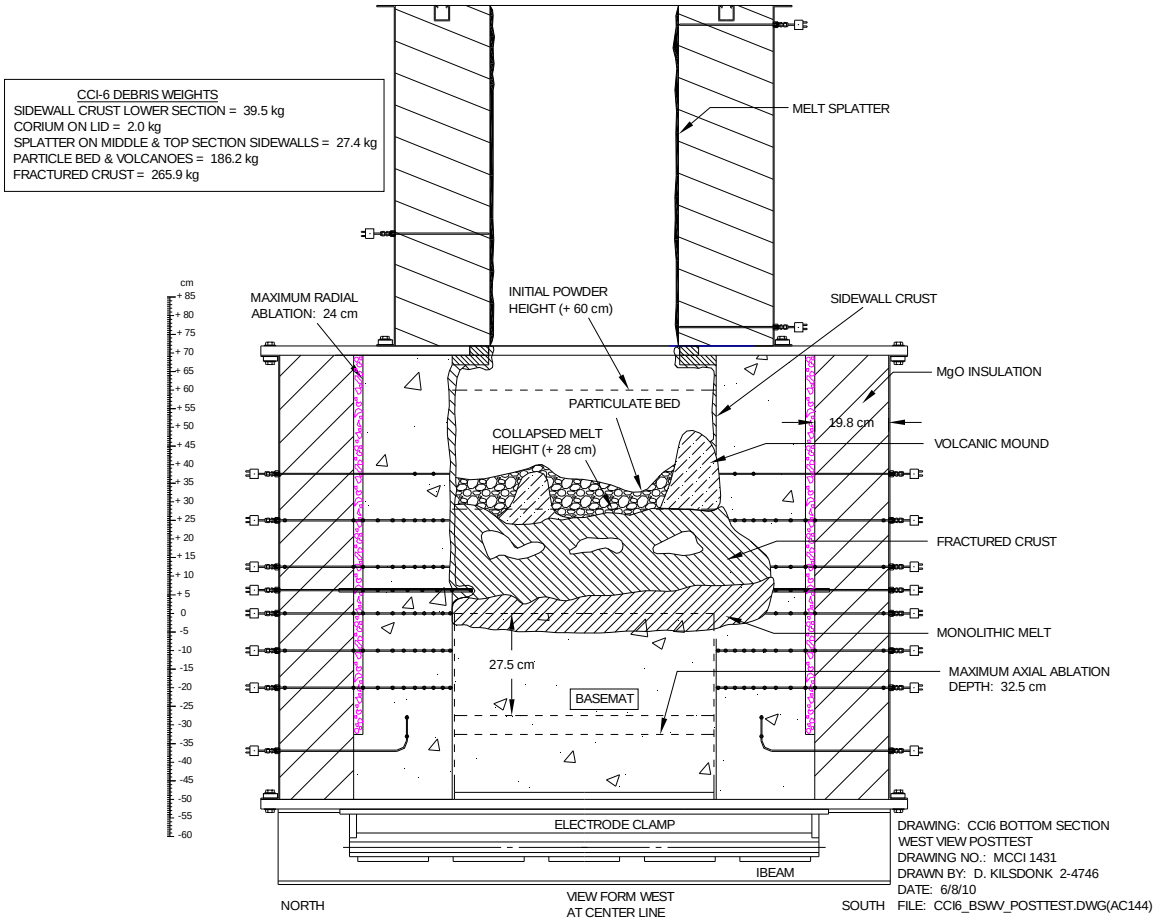

Figure 3-23. Rendering of Posttest Debris Configuration.

Operationally, CCI-6 was carried out according to the planned procedure, with the exception that water was added ~ 40 seconds after the melt pool was formed, as opposed to after cavity ablation was initiated. (Early water addition was performed to reduce the temperature of the gas jet issuing into the cell through the failed test section main steamline.) Thus, the initial cooling behavior was indicative of a corium melt pool containing 6 wt % siliceous concrete interacting with a concrete crucible in which the concrete surfaces were protected by insulating crusts. Despite the relatively low heat transfer rate to the concrete through the crusts, the initial debris cooling rate was quite high (i.e., 5 MW/m^2), and melt eruptions were observed over the first 3 minutes of the melt-water interaction (see Table 3-1). Although cavity ablation was not occurring during this interval, concrete heatup was nonetheless occurring which resulted in the release of concrete decomposition gases. The gas release in turn caused melt eruptions. Due to the low concrete content of the corium the crust dryout limit was relatively high (i.e., > 200 kW/m^2 based on the SSWICS water ingression correlation [17]). Thus, water ingression into fractured crust material may have also contributed to the early high debris cooling rate.

After 10 minutes, onset of axial ablation began. Thereafter, axial ablation proceeded slowly but steadily at a rate of ~ 2 cm/hour over the balance of the test. The lance insertion data suggested that the concrete surface was covered by a 2-3 cm thick crust at ~ 60 minutes into the test sequence, which may explain the slow but steady ablation behavior. The radial ablation characteristics were quite different from the axial case. The sidewall instrument readings show that both walls were initially protected by corium crusts. However, at 21 minutes a rapid ablation burst was initiated on the south concrete wall, leading to an average ablation rate of ~ 2.7 cm/min as the ablation proceeded to a depth of 16 cm before stabilizing. The local heat flux to the siliceous concrete required to sustain this ablation rate is of the order of 2 MW/m^2. Following this transient, additional sidewall ablation was terminated by water ingression at the core/concrete interface.

Data from the experiment further illustrated the local coupling between the cavity erosion behavior and the melt pool thermalhydraulics. In particular, melt temperature measurements indicate that the ablation transient in the south concrete wall was initiated at 21 minutes by failure of the crust that protected that surface during the early phase of the experiment. Over the next six minutes, melt temperatures near the south wall dropped steadily until reaching a plateau at ~ 27 minutes. The plateau occurred at about the same time as the ablation transient in the wall terminated. The data suggest that the sensible energy driving the ablation during this transient was provided by the melt fairly close to the south wall, as opposed to bulk energy extraction from the entire melt volume. In particular, given the measured melt temperature drop adjacent to the wall as well as the known mass of eroded concrete, then a simple energy balance reveals that the energy required to erode the concrete would have been extracted from a melt mass of ~ 340 kg, which amounts to ~ 38 % of the initial melt mass used in the experiment. Another possible explanation[5] for the transient is based on a cement paste liquefaction concept where the siliceous aggregate was only partially melted when the crust disappeared. This relatively cold material was then introduced into the melt pool once the crust failed, causing the temperature decrease. After the aggregate melted, the pool temperature was then able to rise again.

Following the ablation transient, temperature measurements in the concrete indicate that additional ablation was minimal. The lack of bubble-induced convection within the melt from concrete decomposition resulted in large temperature gradients across the extent of the test section that ranged up to 500˚C or more. The disparity was enhanced by the fact that the corium for this test contained a very low initial concrete content. Thus, the melt may have been quite stiff in the measured temperature range, and conduction within the debris would not have been negligible. Under these conditions, large temperature gradients developed. By the end of the experiment, the temperatures varied from 700 to 1680˚C across the extent of the debris.

Heat removal to overlying water over the course of the experiment was substantial; amounting to ~ 1400 MJ by the time power input was terminated at 150 minutes. This level of heat extraction can be compared with the ~ 1080 MJ initial energy content of the melt, as well as the 450 MJ of heat input from DEH during the test. The large degree of heat removal to overlying water is also consistent with both the power supply response and the posttest debris morphology. In particular, the input power fell from ~ 210 kW to ~ 70 kW during the rapid

sidewall ablation phase. Since input power in constant voltage operation is inversely proportional to the size of the electrical conductor, this level of power reduction is consistent with the loss of ~ 65 % of the debris from the melt zone in the form of cooled core material. Furthermore, the posttest debris examinations indicated that over 50 % of the debris had been quenched in the form of a coolable debris configuration by the end of the test (i.e., 186 kg particle bed from eruptions, as well as 266 kg fractured crust from water ingression). Furthermore, the lance insertion sequence indicated that a loose debris structure had been formed by 60 minutes into the experiment sequence which is consistent with early, aggressive debris cooling. In terms of melt eruption characteristics, analysis of the data indicates that the melt entrainment coefficient averaged over the course of the test was 0.04 %. As noted by Bonnet and Seiler [16], this value is in the range where debris cooling and stabilization can be achieved on the basis of melt eruptions alone.

In summary, the CCI-6 was operationally successful, despite early melt through of the main steamline. The debris cooled exceptionally well, particularly in light of the fact that the test was conducted with siliceous concrete which has relatively low gas content. The debris-water heat flux, power supply response, and posttest debris morphology were all consistent with very good cooling. The question naturally arises as to why this test cooled so well relative to previous tests conducted in the OECD/MCCI and MACE experiment programs. Differences between this experiment and those conducted previously include: i) increased scale, ii) early cavity flooding, iii) lowest initial concrete content in the melt (6 wt %), and iv) *no anchored crust* occurred that confounded coolability demonstration in the previous MACE experiment program. Finally, another difference between this test and virtually all tests conducted in the MACE program is that CCI-6 utilized a 2-D concrete crucible, as opposed to the 1-D configuration used in MACE. With respect to cooling mechanisms, the test also demonstrated that melt eruptions are viable for siliceous concrete, and that water ingression into fractured crust material is very effective for low concrete melts. Unfortunately, due to the relatively good cooling that was experienced early on, no data on bottom water injection cooling at large scale was obtained.

4.0 SUMMARY AND CONCLUSIONS

The objectives of CCI-6 were to: 1) carry out a large scale integral-effect test to provide data on core debris coolability under early *top flooding* conditions, and if the corium does not quench during this initial interaction, 2) provide additional data on coolability under *bottom flooding* conditions wherein water is injected into the melt through nozzles cast in the basemat. The overall experiment approach taken to meet these objectives was to: 1) enlarge the test section to minimize scaling distortions, and 2) incorporate an array of water injection nozzles into the core-concrete interaction test apparatus to inject water from below. Specifically, the test section was enlarged to incorporate a 70 cm x 70 cm basemat, and the initial melt depth was increased to 28 cm (900 kg melt mass). The thermite was redesigned to reduce the amount of concrete initially present (i.e., 6 wt %) to better mockup early cavity conditions. Water was intended to be added to the cavity as soon as ablation began. The basemat was redesigned to accommodate an array of water injection nozzles to quench the melt from below if the melt was not quenched earlier and ablation proceeded to 27 cm.

The experiment was operationally successful, despite early melt through of the main steamline. The debris cooled exceptionally well, particularly in light of the fact that the test was conducted with siliceous concrete which has relatively low gas content. The debris-water heat flux, power supply response, and posttest debris morphology were all consistent with very good cooling. The question arises as to why this test cooled so well relative to previous tests conducted in the OECD/MCCI and MACE experiment programs. Differences between this experiment and those conducted previously include: i) increased scale, ii) early cavity flooding, iii) lowest initial concrete content in the melt (6 wt %), and iv) *no anchored crust* occurred that confounded coolability demonstration in the MACE experiment program. Finally, another difference between this test and virtually all tests conducted in the MACE program is that CCI-6 utilized a 2-D concrete crucible, as opposed to the 1-D apparatus used in MACE.

With respect to cooling mechanisms, the test also demonstrated that melt eruptions are viable for siliceous concrete, and that water ingression into fractured crust material is very effective for low concrete melts. Unfortunately, due to the relatively good cooling that was experienced early on, no data on bottom water injection cooling at large scale was obtained.

5.0 REFERENCES

1. M. T. Farmer, D. J. Kilsdonk, S. Lomperski, and R. W. Aeschlimann, “Category 4 Integral Test to Validate Severe Accident Codes: Core-Concrete Interaction Test Six (CCI-6) Test Plan,” OECD/MCCI-2009-TR02, March 2009.

2. M. T. Farmer, D. J. Kilsdonk, R. W. Aeschlimann, and S. Lomperski, “Category 4 Integral Test to Validate Severe Accident Codes: Core-Concrete Interaction Test Six (CCI-6) Data Report,” OECD/MCCI-2010-TR04, June 2010.

3. T. G. Theofanous, C. Liu, and W. W. Yuen, “Coolability and Quench of Corium-Concrete Interactions by Top-Flooding,” MACE-TR-D14, August, 1998.

4. R. E. Blose, J. E. Gronager, A. J. Suo-Anttila, and J. E. Brockman, "SWISS: Sustained Heated Metallic Melt/Concrete Interactions With Overlying Water Pools," NUREG/CR-4727, July 1987.

5. R. E. Blose, D. A. Powers, E. R. Copus, J. E. Brockmann, R. B. Simpson, and D. A. Lucero, "Core-Concrete Interactions with Overlying Water Pools - The WETCOR-1 Test," NUREG/CR-5907, November 1993.

6. H. Nagasaka, M. Kato, I. Sakaki, Y. Cherepnin, Y. Vasilyev, A. Kolodeshnikov, V. Zhdanov, and V. Zuev, “COTELS Project (1): Overview of Project to Study FCI and MCCI During a Severe Accident,” OECD Workshop on Ex-Vessel Debris Coolability, Karlsruhe, Germany, November 15-18, 1999.

7. H. Nagasaka, I. Sakaki, M. Kato, Y. Vasilyev, A. Kolodeshnikov, and V. Zhdanov, “COTELS Project (3): Ex-vessel Debris Cooling Tests,” OECD Workshop on Ex-Vessel Debris Coolability, Karlsruhe, Germany, November 15-18, 1999.

8. M. T. Farmer, B. W. Spencer, D. J. Kilsdonk, and R. W. Aeschlimann, “Results of MACE Corium Coolability Experiments M0 and M1b,” Proceedings of ICONE-8, 8th International Conference on Nuclear Engineering, Baltimore, MD, April 2-6, 2000.

9. M. T. Farmer, D. J. Kilsdonk, and R. W. Aeschlimann, “Corium Coolability under Ex-Vessel Accident Conditions for LWRs,” *Nucl. Eng. Technol*, **41**,575 (2009).

10. B. R. Sehgal, “Light Water Reactor (LWR) Safety,” *Nucl. Eng. Technol*., **38**, 1 (2006).

11. M. T. Farmer, S. Lomperski, D. J. Kilsdonk, and R. W. Aeschlimann, “OECD MCCI Project 2-D Core Concrete Interaction (CCI) Tests: Final Report,” OECD/MCCI-2005-TR05, January 2, 2006.

12. M. T. Farmer, R. W. Aeschlimann, D. J. Kilsdonk, and, S. Lomperski, “2-D Core Concrete Interaction (CCI) Tests: CCI-4 Final Report,” Rev.0, OECD/MCCI-2007-TR06, November, 2007.

13. M. T. Farmer, D. J. Kilsdonk, S. Lomperski, and R. W. Aeschlimann, "CCI-5 Data Report," OECD/MCCI-2009-TR06, November 2009.

14. S. Lomperski, M. T. Farmer, D. Kilsdonk, and R. W. Aeschlimann, "Small-Scale Water Ingression and Crust Strength Tests (SSWICS) SSWICS-12 Design," OECD/MCCI-2008-TR06, October, 2008.

15. D. H. Thompson, M. T. Farmer, J. K. Fink, D. R. Armstrong, and B. W. Spencer, "ACE Phase C Final Report: Volume I-MCCI Thermalhydraulic Results," EPRI/ACE-TR-C42, September, 1997.

16. J. M. Bonnet and J. M. Seiler, "Coolability of Corium Spread Onto Concrete Under Water, the PERCOLA Model," *2nd CSNI Specialist Meeting on Core Debris-Concrete Interactions*," Karlsruhe, Germany, April 1-3, 1992.

17. S. Lomperski, M. T. Farmer, D.J. Kilsdonk, and R. W. Aeschlimann, "Small-Scale Water Ingression and Crust Strength Tests (SSWICS) SSWICS Final Report: Thermal Hydraulic Results," OECD/MCCI-2005-TR03, June 2005.